Environmental dynamics during the Paleocene–Eocene thermal maximum (PETM) in the northeastern Peri-Tethys revealed by high-resolution micropalaeontological and geochemical studies…

Article *in* Palaeogeography Palaeoclimatology Palaeoecology · May 2016

Impact Factor: 2.34 · DOI: 10.1016/j.palaeo.2016.05.006

6 authors, including:

Ekaterina Shcherbinina

Russian Academy of Sciences

51 PUBLICATIONS **207** CITATIONS

SEE PROFILE

Yu. O. Gavrilov

Russian Academy of Sciences

45 PUBLICATIONS **162** CITATIONS

SEE PROFILE

Alina I. Iakovleva

Geological Institute

40 PUBLICATIONS **257** CITATIONS

SEE PROFILE

G. N. Aleksandrova

Russian Academy of Sciences

48 PUBLICATIONS **155** CITATIONS

SEE PROFILE

Palaeogeography, Palaeoclimatology, Palaeoecology 456 (2016) 60–81

Contents lists available at ScienceDirect

Palaeogeography, Palaeoclimatology, Palaeoecology

journal homepage: www.elsevier.com/locate/palaeo

Environmental dynamics during the Paleocene–Eocene thermal maximum (PETM) in the northeastern Peri-Tethys revealed by high-resolution micropalaeontological and geochemical studies of a Caucasian key section

Ekaterina Shcherbinina *, Yuri Gavrilov, Alina Iakovleva, Boris Pokrovsky, Olga Golovanova, Galina Aleksandrova

Geological Institute of the Russian Academy of Sciences, Pyzhevsky 7, 119017 Moscow, Russia

ARTICLE INFO

Article history:
Received 12 August 2015
Received in revised form 30 April 2016
Accepted 4 May 2016
Available online 10 May 2016

Keywords:
Paleocene–Eocene Thermal Maximum
Nannofossils
Dinocysts
Organic matter
Carbon and oxygen isotopes

ABSTRACT

The sedimentary record of the Paleocene–Eocene Thermal Maximum (PETM) in the wide epeiric sea of the NE Peri-Tethys contains a sapropelitic bed (SBD) characterized by a specific microfossil assemblage and negative oxygen and carbon isotope excursions (CIE). New results obtained from a high-resolution sampling of this interval in the Kheu section, central Caucasus, allows us to explore the succession, interrelationships and consequences of global and regional palaeoenvironmental events during the PETM. The CIE apparently lasted twice as long as the SBD accumulation period; thus, the SBD represents a response to the early and most dramatic phase of the PETM related to rapid transgression and greatly enhanced eutrophication of the basin. The lithological architecture of the SBD represents four bands, each of which consists of a dark, low-calcareous TOC-rich clay and relatively paler calcareous clays. The highest TOC concentrations are found in the lower and upper bands of the SBD; however, the lower band mostly consists of basinal organic matter, while the upper band represents mixed, basinal and terrestrial, organic matter. Pre-PETM events include the initial evolution of the *Rhomboaster* nannofossil lineage with the early first appearance of a short-arm species, relatively reduced calcareous plankton productivity, changes in the ratios of dinocyst ecological groups, and minor fluctuations in $\delta^{13}C$ and $\delta^{18}O$. The onset of the CIE corresponds to the base of the SBD, which exhibits a dramatic decrease in total nannofossil abundance and an increase in total dinoflagellate abundance, the occurrence of "excursion taxa" of nannofossils (rhomboasters, asymmetric discoasters) and dinocysts (*Axiodinium augustum*, *Epelidinium pechoricum*), and significant variations in the species ratios of both nannoplankton and dinoflagellate communities, with widespread dominance of warm-water and eutrophic species. Above the SBD but during the late phase of CIE, the nannofossil abundance and species composition show a slight recovery, but most Paleocene taxa become extinct during the CIE recovery. *Apectodinium* spp. significantly decrease in abundance above the SBD, but rare specimens of *Ax. augustum* persist higher in the section after the end of the CIE. Thus, the major extinction of the Paleocene nannofossil taxa occurs after the termination of the most critical conditions during the CIE recovery phase, while the dinocyst "excursion taxa" survive even later.

1. Introduction

During the Cretaceous to early Paleogene, the northern Caucasian basin represented a relatively deeper part of vast shelf area of the Peri-Tethys barriered from the Tethys by a wide island or archipelago in different epochs (Fig. 1). By the end of the Paleocene, the central northern Caucasus appeared to be the deepest part of the basin, which was characterized mainly by calcareous-siliciclastic sedimentation and abundant and diverse calcareous microbiota (nannoplankton and planktonic foraminifera).

The Paleocene/Eocene transition in the north-eastern Peri-Tethys is marked by a sapropelitic bed (SBD) that was discovered and correlated from the Caucasus to Central Asia in the early 1980s by N. Muzylöv, who considered it to be a marker of an important supra-regional geological event and correlative level (Muzylöv, 1994). Subsequently, the SBD was found to correspond to the global biospheric event known as the Paleocene–Eocene Thermal Maximum, or PETM (Gavrilov et al., 1997; Gavrilov et al., 2003). This intense Cenozoic palaeoecological crisis at ~55.7–56.0 Ma (Hilgen et al., 2010; Charles et al., 2011) involved

* Corresponding author.
E-mail address: katuniash@gmail.com (E. Shcherbinina).

http://dx.doi.org/10.1016/j.palaeo.2016.05.006
0031-0182/

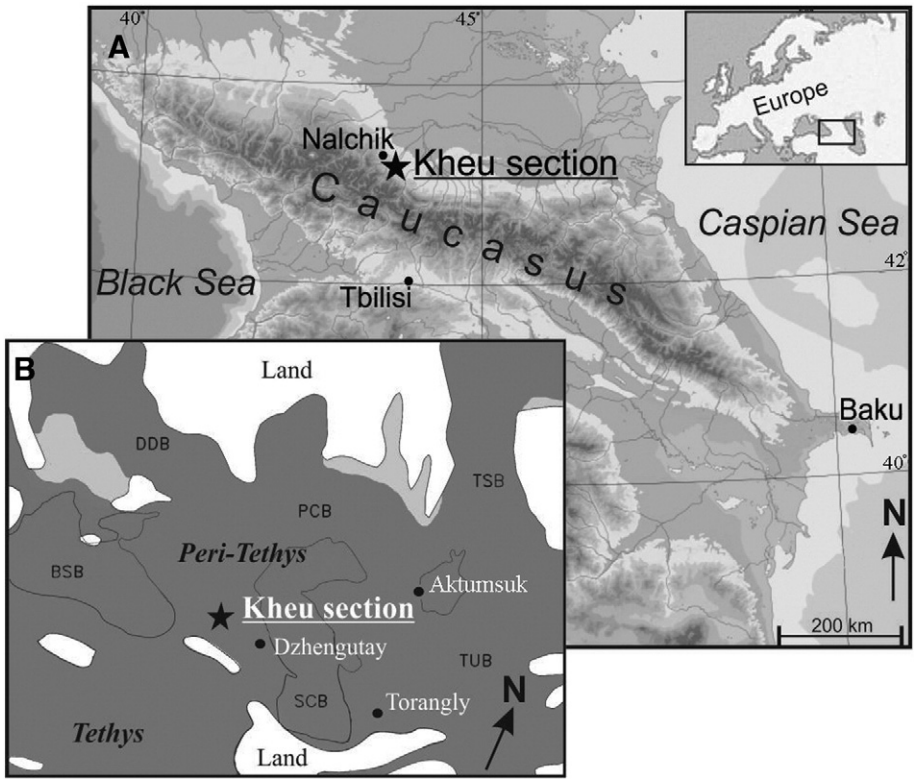

Fig. 1. Schematic map of the study area. A) Regional map showing the location of the Kheu section; the geographic position of the enlarged area is shown in the inset. B) Location of the Kheu section on the palaeogeographic map (Kazmin and Natapov, 1998, modified). Peri-Tethyan basins: BSB — Black Sea Basin, GCB — Greater Caucasian Basin, DDB — Dnieper–Donets Basin, PCB — Peri-Caspian Basin, SCB — Southern Caspian Basin, TUB — Turanian Basin, TSB — Turgay Straight Basin.

dramatic climatic warming, when temperatures rose globally from 5 to 9° during a period of 200 Ky, significant changes in the global carbon budget expressed by a broad negative carbon isotope excursion (CIE), turnovers in marine and terrestrial biotas and possible reorganization of oceanic circulation and chemistry (e.g., Kenett and Stott, 1991; Dickens et al., 1995; Fricke et al., 1998; Bains et al., 1999; Beerling, 2000; Zachos et al., 2005; Pagani et al., 2006; Sluijs et al., 2007; Smith et al., 2007; Alegret et al., 2010; Gibbs et al., 2010; Higgins, 2012; Handley et al., 2012; Pälike et al., 2012; Speijer et al., 2012; Dunkley Jones et al., 2013; Penman et al., 2014, a.o.). This dramatic event was associated with significant sea-level changes (Gavrilov et al., 1997; Speijer and Wagner, 2002; Pujalte et al., 2014; Sluijs et al., 2008; Egger et al., 2009; Handley et al., 2011) and major tectonic events and volcanic eruptions (Eldholm and Thomas, 1993; Svensen et al., 2004; Dickson et al., 2015; Aarnes et al., 2015). In the sedimentological record of deep oceanic settings, CIE corresponds to carbonate dissolution horizon (e.g., Bralower et al., 1997; Thomas et al., 2000). At the same time, the wide occurrence of oxygen-depletion conditions in the northern and southern Peri-Tethyan basins led to the accumulation of TOC-rich sediments in these expanded epeiric basins (Kodina et al., 1995; Gavrilov et al., 1997; Speijer et al., 1997; Khozyem et al., 2013, 2014).

The previous results from the north-eastern Peri-Tethys indicate the SBD is characterized by high TOC content of up to 6–8% (up to 25% in Tadjik Depression, Central Asia, Gavrilov et al., 2003), a large negative carbon isotope excursion detected in both calcium carbonate and organic matter, the extinction of benthic foraminifera, a drop in calcareous microplankton productivity, the occurrence of the calcareous nannofossil "excursion taxa" *Rhomboaster* spp. and asymmetric discoasters (Gavrilov et al., 2000, 2003; Stupin and Muzylöv, 2001) and an acme of the dinocyst genus *Apectodinium* (Akhmetiev and Zaporozhetz, 1996; Crouch et al., 2003). A shift from aerobic and oligotrophic to anaerobic and eutrophic benthic foraminiferal communities at the onset of the PETM is evident in the eastern part of the basin (Torangly section, Turkmenistan; Speijer et al., 1997). Radiolarians and diatoms become common across the Paleocene/Eocene transition in the Kheu section, although they are extremely rare in the adjacent sediments (Radionova et al., 2009). The isorenieratene biomarkers in the eastern part of the basin suggest the anoxic environment during the SBD accumulation (Kodina et al., 1995). All of these features indicate drastic palaeoecological stress across this huge shelf basin during the SBD accumulation.

Recent sedimentological and geochemical studies of the SBD in the Kheu section show significant TOC enrichment (up to 7–9%) inhomogeneously concentrated within the bed and an inverse relationship between TOC and calcium carbonate. Numerous trace elements (Fe, S, P, Co, Ni, V, Cr, Cu, etc.) are 5–10 times more concentrated in the SBD than in the surrounding sedimentary layers. Additionally, molybdenium is more than 30 times more concentrated, while manganese generally displays reduced concentrations (Gavrilov and Muzylöv, 1991; Gavrilov et al., 1997). Rock-Eval II pyrolysis data reveal the dominance of basinal organic matter with admixed terrestrial organic matter in the SBD (Kerogen II–III, HI = 257–290). Total nannofossil abundance decreases significantly within the SBD, and *Toweius*, *Fasciculithus* and warm-water discoasters dominate the nannofossil assemblage. Benthic foraminifera decline dramatically within the SBD, and only those taxa that could tolerate low ambient oxygenation persisted at low abundance. Planktonic foraminifera also decline in abundance and are dominated by subbotinids in the lower part of the SBD and by warm-water acarinids and morozovellids toward the top of the SBD (Stupin, 2008). Fish remains are frequent in the SBD and include epipelagic species and newly arising taxa (Bannikov and Carnevale, 2012).

The accumulation of the SBD was likely caused by dramatically increased algal, phytoplankton and bacterioplankton productivity due to massive nutrient discharges from adjacent wetlands into the basin

during rapid, large-scale sea-level fluctuations (Gavrilov et al., 1997, 2003).

Despite this array of information about the nature and features of the SBD, several important aspects of the general evolution of the north-eastern Peri-Tethys during the PETM remain unclear, particularly (1) the chronological order of onsets of the CIE, TOC-rich sediment accumulation and microplankton community turnover; (2) the duration of these events and their relationships; and (3) the tempo of the onset and termination of the PETM in the basin. For a better understanding of the environmental dynamics in the Caucasian basin during the PETM, particularly its onset and recovery, and to elucidate the consequences of the various events involved, we performed a high-resolution study of the SBD and adjacent sediments from a key section exposed along the Kheu River near the village of Gerpegezh, Kabardino-Balkaria Republic, northern Caucasus (Fig. 1). The sampling obtained in this study was much more detailed than previous surveys (e.g. Gavrilov et al., 1997, 2003; Stupin and Muzylöv, 2001) and thus reveal many additional features of PETM development in the basin.

2. Lithostratigraphy

The Kheu section represents the most complete Paleogene succession in the southern Russia (Gavrilov et al., 2000). The upper Paleocene sediments are composed of greenish marls attributed to the Nalchik Formation (~40 m), which onlaps Danian limestones and marlstones by erosional surface. The 0.58-m-thick SBD is intercalated in the uppermost part of the Paleocene interval of the section (~4 m below the top of the Nalchik Formation) (Fig. 2). Several layers can be recognized in the sediments embedding the SBD and within the SBD, The Layer 1 (from −3.3 to −1.4 m below the SBD) and the Layer 3 (from −1.36 to −0.15 m) (Fig. 3) are soft, homogenous, borrowed greenish-grey marls. They are separated by few centimetre thick disrupted interval (Layer 2), representing the layer (possibly, bentonite) destroyed more likely by slope slumping during sea-level fall or uplift rising. We found the bentonite interlayer of the same stratigraphic position in the Dzhengutay section, Eastern Caucasus. The Layer 2 was omitted in sampling because of its strong disruption evidently obscured its primary lithological and, possibly, geochemical features. The SBD is underlain by 12-cm-thick, brown, non-calcareous clay lack nannofossils and foraminifera (Layer 4).

The SBD represents dark, grey to black, thinly laminated non-calcareous and low-calcareous clays rich in fish scale (up to 1 cm in diameter and more) and containing fish remnants, shark teeth (up to 1 cm) and pyrite concretions occurred mostly in the darkest parts of the SBD. We distinguished four bands (numbered from I to IV in the Fig. 3) within the SBD (Layer 5). They are made up of dark, thinly laminated, non-calcareous, mostly lack burrows clays rich in organic matter at the base of each band and paler, calcareous clays at the top. The level −0.28 m below the SBD contains small pyrite concretions (2–3 cm); similar concretions are spread in the lower and middle parts of the SBD.

The SBD is overlapped by grey calcareous clay (Layer 6, ~4.5 m) gradually giving way to siliciclastic Abazinsk Formation.

3. Material and methods

We sampled 3 m of sediments underlying the SBD and 2 m of the overlying sediments at a spacing of ~10–15 cm, and we collected the SBD as an oriented block and divided it into ~1.5–2-cm-thick lamina in the laboratory. The TOC, calcium carbonate content, carbon and oxygen isotopes and nannofossil assemblages were analysed from each of the samples obtained (26 from the adjacent sediments and 31 from the SBD). Palynomorphs were studied with a lower resolution: 13

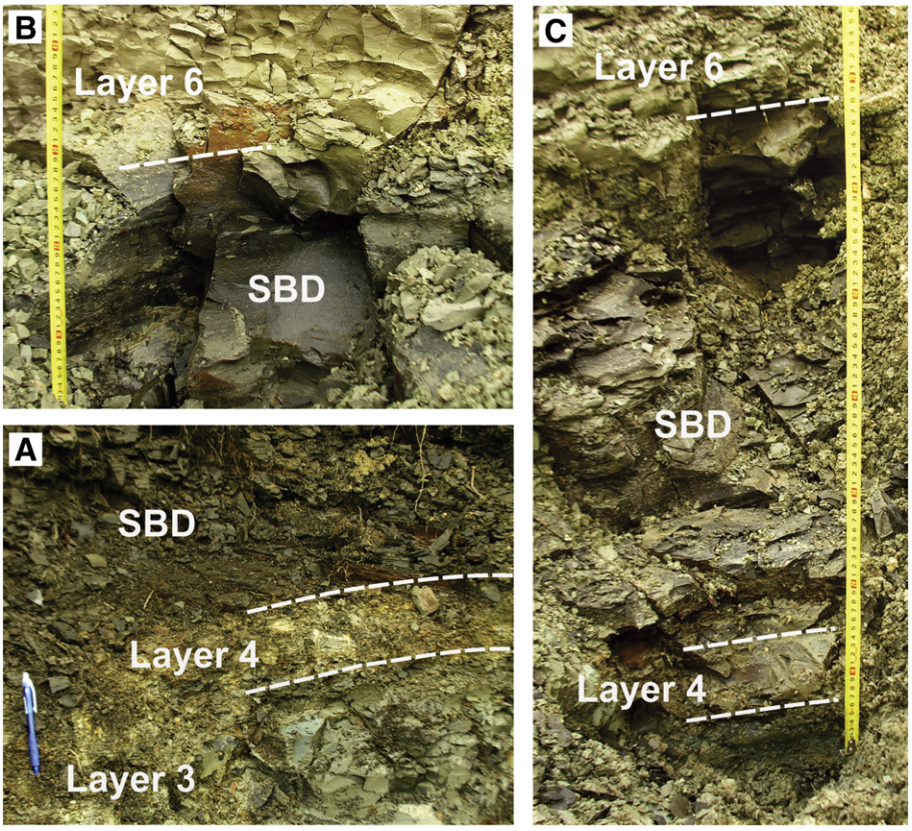

Fig. 2. Field photographs of the sapropelitic bed in the Kheu section. A) lower boundary of the SBD and underlying non-calcareous clay (Layer 4); B) upper boundary of the SBD and overlying calcareous clay (Layer 6); C) general view of the SBD and surrounding sediments. Scale is shown in the measure tape.

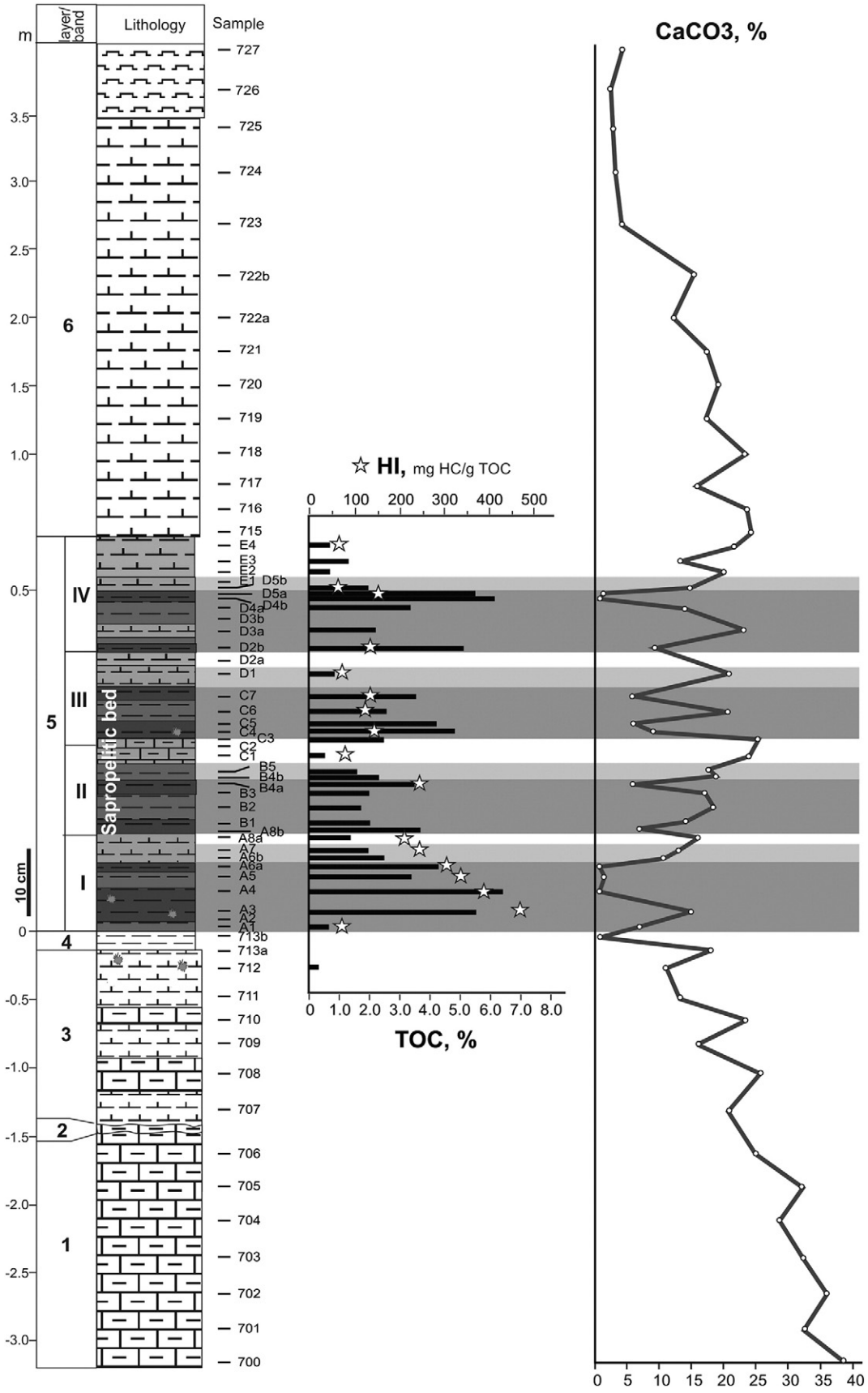

Fig. 3. Distribution of TOC and $CaCO_3$ across the Paleocene/Eocene transition in the Kheu section. Note the different scales of the SBD and the embedding sediments. See Fig. 4 for symbols.

samples from the underlying uppermost Thanetian greenish marl and 23 samples from the SBD and its overlying sediments.

Nannofossils were examined at 1250× magnification under the polarizing light microscope Olympus BX-41. Smear slides were prepared from raw sediment using standard techniques (e.g., Bown and Young, 1998). The percentages of nannofossil taxa were usually counted from 300 specimens, but in a few samples from the SBD, containing rare and taxonomically poor nannofossils, percentages were counted from 100 specimens.

Palynomorphs were concentrated according to the standard palynological techniques of the Russian Academy of Sciences. Samples were (1) processed with 10% hydrochloric acid until the calcium carbonate was dissolved; (2) processed with 10% tetrasodium pyrophosphate (Na4P2O7 × 10H2O) to disperse the clay; (3) washed several times to eliminate the argillaceous compounds; (4) centrifuged with a heavy liquid (K2CdJ4) with a specific gravity of 2.25; (5) washed in water and then treated with 10% hydrofluoric acid until the siliceous matter was dissolved; and (6) boiled with 10% hydrochloric acid to remove fluoro-silicate compounds. The material was not sieved. The residues were mounted on glass slides using glycerine jelly. The quantitative analysis of the palynological samples involved two steps. First, a minimum of 100–200 palynomorphs were counted and grouped into 10 broad categories (dinocysts, acritarchs, prasinophytes, green algae, fungi, angiosperms, conifers (Pinaceae, Cupressaceae), spores and unknown palynomorphs). Second, a minimum of 200 dinocysts were counted, whenever possible. The remaining material was scanned for rare dinocyst taxa. The quantitative results are presented as percentages of the total count.

The calcium carbonate composition was determined using X-ray diffractometry. Chemical analysis of $CaCO_3$ was made using a gravimetric technique; its content was calculated after the treatment of sediments with HCl and CO_2 absorption in Ascarite. TOC was analyzed gravimetrically after oxidation of organic matter with chromium trioxide. Additionally, TOC content was obtained from Rock-Eval pyrolysis. The application of different analytical methods caused minor gaps in TOC values. We used the average values for samples with double analytical data of TOC concentrations. The pyrolytic analysis of TOC composition (hydrogen index, HI) was performed with Rock-Eval 2 equipment in

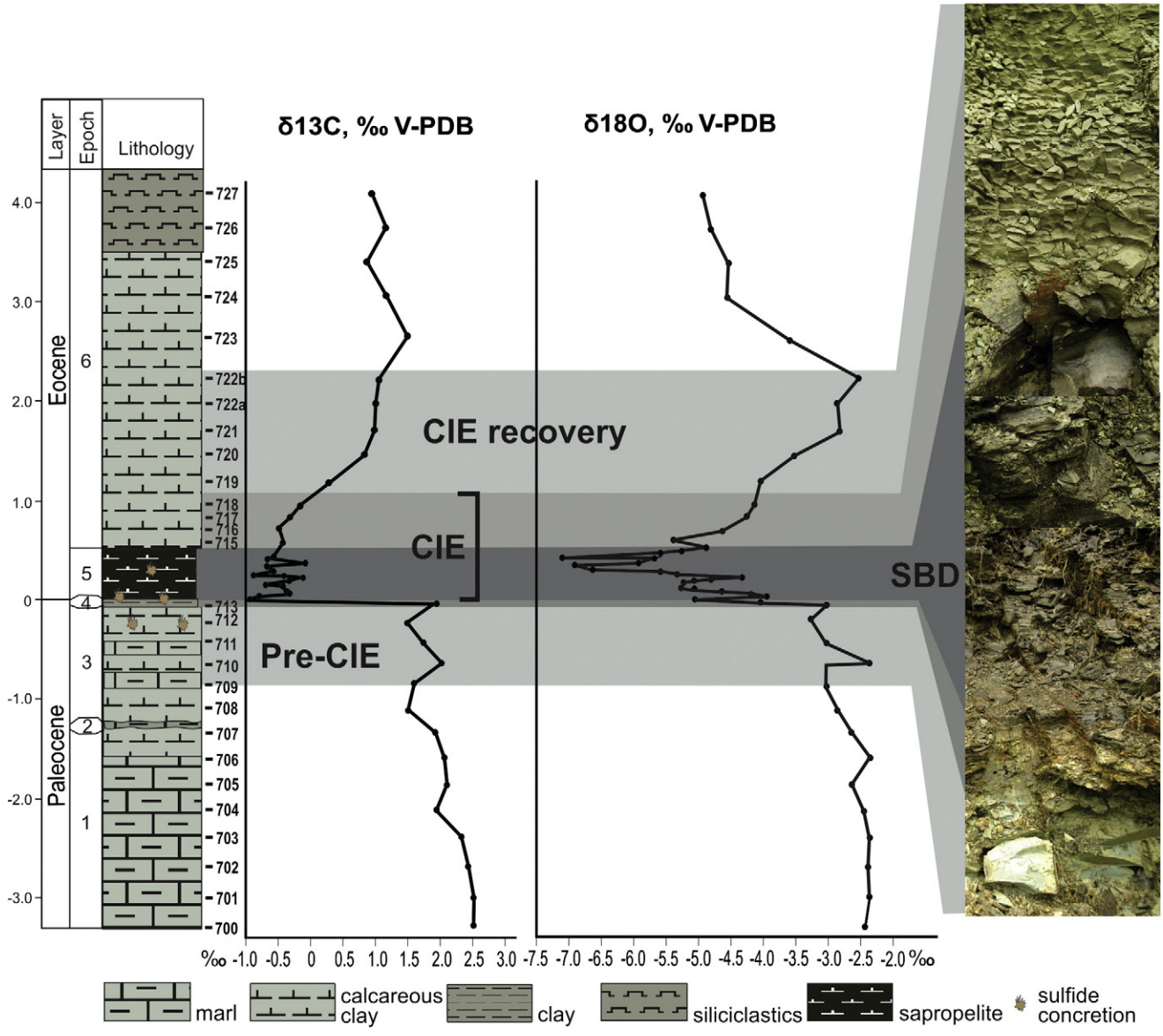

Fig. 4. Carbon and oxygen isotope curves across the Paleocene/Eocene transition in the Kheu section made from bulk carbonate analysis.

the Institute of Geology and Development of Combustible Mineral Resources. Calcite composition of the carbonate component is inferred from XRD analysis.

Carbon and oxygen isotope analysis was made from bulk carbonate with the equipment designed by the Thermoelectron Corporation that included the Delta V Advantage spectrometer and Gas Bench II device. The samples and standards (KH 2, IAEA CO 1, and NBS 19) were decomposed using H_3PO_4 at the temperature of 50 °C. The $\delta^{13}C$ and $\delta^{18}O$ values are given in pro mille (‰) relative to the V-PDB standard. Accuracy (reproducibility) of $\delta^{13}C$ and $\delta^{18}O$ measurements was ± 0.2‰.

4. Results

4.1. Calcium carbonate content and TOC

The calcium carbonate component of the SBD and adjacent marly sediments is composed by calcite only. The greenish marls and calcareous clays of Layers 1 and 3 are mostly poor in TOC (<0.1%) in the Kheu section. A low TOC value (0.26%) is found in sample 712 (~0.28 m below the SBD), from the level containing pyrite concretions (see Fig. 3). The $CaCO_3$ concentration progressively decreases from the Layer 1 to the Layer 3 (from 38% to 11%, respectively) toward the base of the SBD. It fluctuates markedly in the Layer 3 and drops to zero in the yellowish-brown clay underlying the SBD (Layer 4). The highest TOC concentrations are found in the non-calcareous clays at the base and top of the SBD (Bands I and IV, 6.3 and 6.2% TOC, respectively). The highest $CaCO_3$ content within the SBD corresponds to its middle (Bands II and III), forming the paler, slightly burrowed portion of the bed. The lithological bands within the SBD demonstrate higher TOC concentrations in the "dark" members and much lower values in the "pale" members. The TOC concentrations within the "dark" parts of each band are irregular. In the Bands II, III and IV, the bases and tops of "dark" members exhibit the highest TOC concentrations, while their middle parts are characterized by lower values. The Band I shows inversed TOC distribution: the highest TOC values are found in the middle of its "dark" part. Generally, TOC and $CaCO_3$ are inversely correlated within the SBD, except in the lower Band I, where the base of the dark layer is lack calcareous microfossils, but enriched in micarb.

The TOC composition inferred from the hydrogen index (HI) suggests the presence of terrestrial organic matter prior to the SBD accumulation (HI = 75 mg HC/g TOC, Kerogen III), but the drastic increase in HI at the base of the SBD (HI = 384–469 mg HC/g TOC, Kerogen II) implies dramatically enhanced basin productivity during the initial phase of the SBD accumulation. The later phases, Bands II to IV, are characterized by a mixture of terrestrial and basin organic matter within the "dark" part of each band (HI = 131–237 mg HC/g TOC) and mostly terrestrial organic matter in the "pale" members and overlying sediments (HI = 62–102 mg HC/g TOC). This pattern indicates variation in the source of organic matter during the SBD accumulation, and the two TOC peaks within the SBD have distinctly different origins.

The $CaCO_3$ concentrations first recover (up to 24.5%) through a ~1.9-m-thick interval of the grey clayey marl of Layer 6 (from 0.8 m) and then progressively decline up-section (above the sample 723), dropping to 2.9% at 3.45 m (sample 725), near the transition to overlying siliciclastic and biosiliceous sediments of the Abazinsk Formation (Gavrilov et al., 2000).

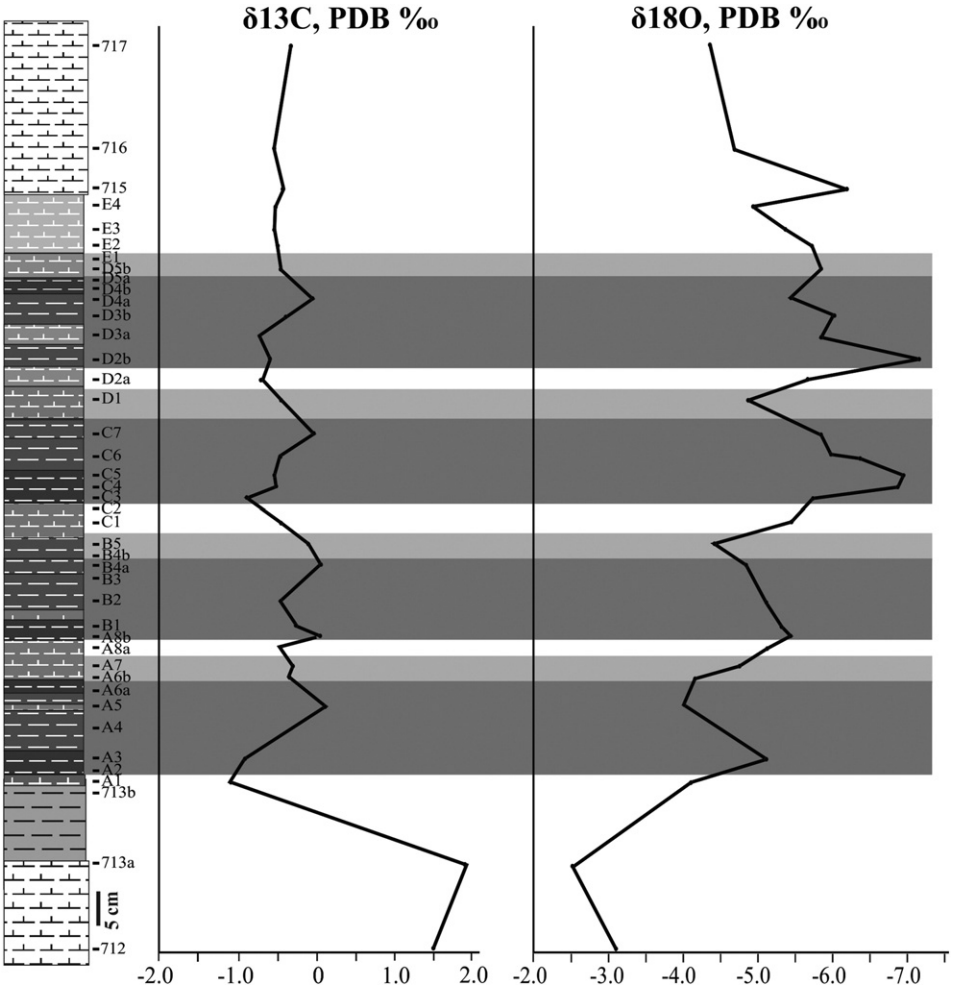

Fig. 5. Enlarged graphs of δ13C and δ18O within the SBD (from −0.18 m to 0.75 m).

4.2. Carbon and oxygen isotopes

The sediments underlying the SBD (Layers 1 and 3) show a gradual decrease in $\delta^{13}C$ from ~2.5‰ to ~1.5‰ (Fig. 4). Minor fluctuations (0.5‰ in magnitude) appear from 0.7 m below the SBD (sample 710) and correspond to the variation in $CaCO_3$ content (see Fig. 3), indicating environmental instability and possibly changes in basin productivity before the onset of the main CIE. The gradual negative trend in $\delta^{18}O$ below the SBD suggests progressive warming with short-lived relative decrease in temperature at the level of sample 710.

A dramatic decline in $\delta^{13}C$ of bulk sediment (~3‰) occurs at the base of the SBD that marks the onset of CIE and the Paleocene/Eocene

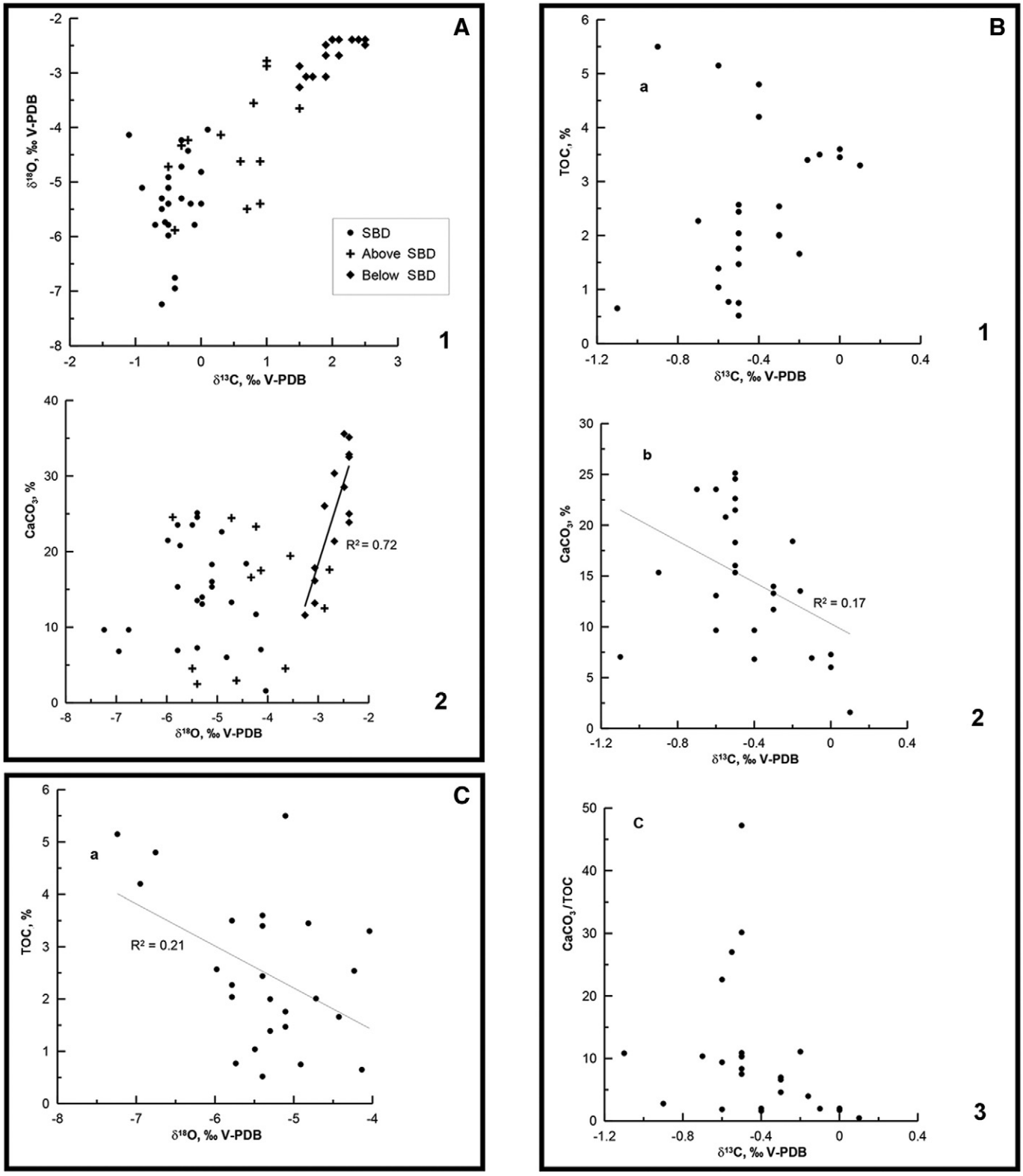

Fig. 6. The correlation diagram of TOC and $CaCO_3$ values and $\delta^{13}C$ and $\delta^{18}O$: A1 — $\delta^{13}C$ vs. $\delta^{18}O$; A2 — $\delta^{18}O$ vs. $CaCO_3$; B1 — $\delta^{13}C$ vs. TOC; B2 — $\delta^{13}C$ vs. $CaCO_3$; B3 — $\delta^{13}C$ vs. $CaCO_3$/TOC; C — $\delta^{18}O$ vs. TOC.

boundary (Aubry and Ouda, 2003). Low $\delta^{13}C$ values are found throughout the SBD, with variations of less than 1‰ in magnitude (Fig. 5). Relatively isotopically heavier values are associated with the tops of the "dark" members.

The most negative $\delta^{13}C$ values within the SBD mainly correspond to the bases of the lithological bands, except in the Band II (from 0.24 m to 0.43 m, the base of the relatively more calcareous middle part of the SBD, corresponding with the onset of increased terrestrial organic-matter input), in which the most negative $\delta^{13}C$ value is found in the middle part. The most negative values within $\delta^{13}C$ excursion were also obtained recently in the middle part of the SBD from the carbon isotope analysis of TOC (Gavrilov et al., 1997). The non-calcareous intervals (samples 713b, A2, A4, A6a, D4b, and D5a) in the lower and upper parts of the SBD do not provide reliable isotope data; those that are most enriched in TOC, evidently corresponding to the strongest environmental perturbations and are missing in the carbon- and oxygen-isotope curves. Above the SBD, $\delta^{13}C$ values remain low, eventually exceeding the isolated, relatively positive peaks within the SBD above sample 718 (~1.02 m). Therefore, this level is considered the upper limit of the CIE. The recovery from the CIE is gradual; the pre-excursion $\delta^{13}C$ values recur at ~3.0 m (~1.9 m above the SBD), but $\delta^{13}C$ declines again above this level to 0.6–0.8‰ and remains within this lower range throughout most of the early Eocene.

The $\delta^{18}O$ curve shows a similar trend: $\delta^{18}O$ decreases below the SBD and rhythmically varies with four bands. The drop in $\delta^{18}O$ at the base of the SBD is slightly lagged compared to that of $\delta^{13}C$ and reaches its maximum (sample A3) a few centimetres above the base of the main CIE (sample A1), with a maximum negative excursion of ~2.6‰. The fluctuations of $\delta^{18}O$ correspond even more closely to the lithological bands within the SBD than those of $\delta^{13}C$, showing more negative values at the base of each band. The recovery of $\delta^{18}O$ occurs much more rapidly than that of $\delta^{13}C$, and the pre-CIE values are reached at ~1.6 m above the SBD. This recovery is evidently related to renewed cooling after the end of the PETM. Farther up-section, however, $\delta^{18}O$ declines again, suggesting a new phase of relative climatic warming.

To define the reliability of the carbon and oxygen isotope analysis in the low-calcareous sediments rich in TOC, we made the estimation of the relationship between TOC and $CaCO_3$ values and $\delta^{13}C$ and $\delta^{18}O$. In the coordinates $\delta^{13}C$ – $\delta^{18}O$ (Fig. 6A-1), there is a positive correlation, which can be a result of 1) increased diagenetic alteration within the SBD comparing to embedding sediments, 2) increased fresh-water input into the basin during the SBD formation and 3) the relationship between climatic warming and changes in the global carbon cycle during PETM. A good correlation between $\delta^{18}O$ values and $CaCO_3$ content is found in the carbonates of the sediments underlying the SBD (Layers 1 and 3), whereas there is no correlation within the SBD and overlying sediments of Layer 6 (Fig. 6A-2).

The most negative values and dramatic variations of $\delta^{13}C$ caused by diagenetic alteration, more likely, should be related to the calcareous component of the SBD, taking into consideration the large fractionation of carbon isotopes between TOC and $CaCO_3$ and variations in the TOC concentrations. However, the $\delta^{13}C$ variations in the TOC-rich sediments of the SBD do not exceed 1‰ (−1.1…0.1‰). At the same time, there is no correlation between $\delta^{13}C$ and TOC values (Fig. 6B1) and between $\delta^{13}C$ and the ratio $CaCO_3$/TOC (Fig. 6B3). There is a weak negative correlation between $\delta^{13}C$ and $CaCO_3$ values (Fig. 6B2) that does not support the relation of the carbon isotope composition with the TOC oxygenation during diagenesis.

The weak positive correlation is found between $\delta^{18}O$ and TOC values (Fig. 6C), which indicates the possibility of weak depletion of the carbonate fraction in the ^{18}O in the most enriched in TOC sediments, but this correlation is based on the results from three samples with lowest $\delta^{18}O$ values (7 ± 0.2‰). In the most samples, there is no correlation between $\delta^{18}O$ and TOC ($\delta^{18}O = -4.0\ldots-6.0$‰). Thus, geochemical criteria do not suggest significant diagenesis effect on the carbon and oxygen isotope composition.

4.3. Nannofossils

4.3.1. Biostratigraphy

The nannofossil assemblages of the upper part of Nalchik Formation below the SBD are abundant, diverse and moderately to well preserved (Plates I and II). A series of first occurrences (FO) are detected prior to and during the SBD accumulation, while many last occurrences (LO) characterize the later stages of the CIE (above the SBD) and the recovery phase (Fig. 7). The FOs of *Blackites solus* and *Zygrhablithus bijugatus* are found at −2.65 and −2.35 m below the SBD, respectively. These species are not present in the pre-CIE interval and the most part of the SBD, but reappear in the uppermost part of the SBD. The first specimens of *Coccolithus bownii*, which is believed to be an "excursion taxon" (Bown and Pearson, 2009), are found in the Kheu section prior to the PETM, from the level of the sample 705 at −1.80 m below the SBD and persist to be presented in low abundance over the whole studied interval. The first species of the *Rhomboaster* lineage, *Rhomboaster intermedia*, first occurs at −0.65 m below the SBD. Similarly, this species appears below the PETM level in the Caravaca (Romein, 1979) and Zumaya (Alegret et al., 2009) sections in Spain.

Above Layer 2, the nannofossil abundance tends to decline (Fig. 8) in parallel with the drop in $CaCO_3$, and nannofossils become more poorly preserved. The FO of rare short-arm rhomboasters (*Rhomboaster cuspis*) at −0.7 m below the SBD and prior to the CIE (sample 710) is remarkable and coincides with the broader, albeit relatively small, fluctuations in $\delta^{13}C$ during the pre-CIE phase (see Fig. 4). This level is defined as the lower boundaries of the NP9b and CP8a subzones. Nannofossils are absent in the brown clay underlying the SBD (Layer 4) and the lowermost part of the SBD (samples A1–A6a, the "dark" member of the Band I). Long-arm rhomboasters, *Campylosphaera eodela*, *Pontosphaera pulchra* and *plana* first occur just above this interval (see the inset in the lower part of Fig. 7). Asymmetric discoasters (*Discoaster araneus*/*Discoaster anartios*) are found few centimetres above (Sample A8, 0.14 m). The co-occurrence of rhomboasters and asymmetric discoasters (so-called "excursion taxa") identifies the RD assemblage (Kahn and Aubry, 2004; Aubry and Salem, 2012), which was found at the base of the CIE in Egypt and used as an alternative marker of the NP9b subzone.

The FO of *Discoaster mahmoudii* in the uppermost part of the SBD (Sample E2, ~0.5 m) apparently coincides with its FO in the Untersberg section, Austria, where there are no TOC-rich sediments but where this species first occurs within the CIE (Egger et al., 2005). The FO of *D. mahmoudii* was recently suggested as the base of NP9c subzone (Aubry and Salem, 2012). This level is close to FO of *Rhomboaster spineus* and LO of *D. araneus*. In Kheu section, the LO of *D. araneus* is found above the FO of *D. mahmoudii*.

The most "excursion taxa" successively become extinct during the recovery phase of CIE, and only rare specimens of short arm rhomboasters are found above it up to the level ~ 3.45 m above the SBD.

The recent study of Agnini et al. (2014) suggested the top of *Fasciculithus richardii* group as the base of lowermost Eocene CNE1 zone and the top of *Fasciculithus tympaniformis* is used as the base of CNE2 zone. In the Kheu section, the some species of *F. richardii* group (*F. alanii*, *F. lillianae*, *F. mitreus*) show their LOs below the SBD, while *F. richardii* and *F. thomasii* remain present within the SBD and the last representative of this group *F. schaubii* has LO at the level of the late stage of CIE (sample 721, 1.75 m). The last fasciculiths (*F. tympaniformis*, *F. involutus* and *F. sidereus*) are found at the level of crisis termination (sample 723, 2.45 m). The survival of fasciculiths after the end of the PETM and their persistence in minor abundance for a short time after CIE termination are evident in many Tethyan sections in Italy (Galeotti et al., 2000), Spain and Egypt (Monechi et al., 2000) and the Southern Ocean (Angori et al., 2007; Raffi et al., 2009), suggesting that evolutionary extinction of this taxon was not directly linked to the PETM, albeit its effect was really dramatic. The typical Paleocene taxa, such as *Heliolithus*, *Neochiastozygus*, *Fasciculithus*, *Placozygus sigmoides* and many species of *Toweius* recovered after crisis

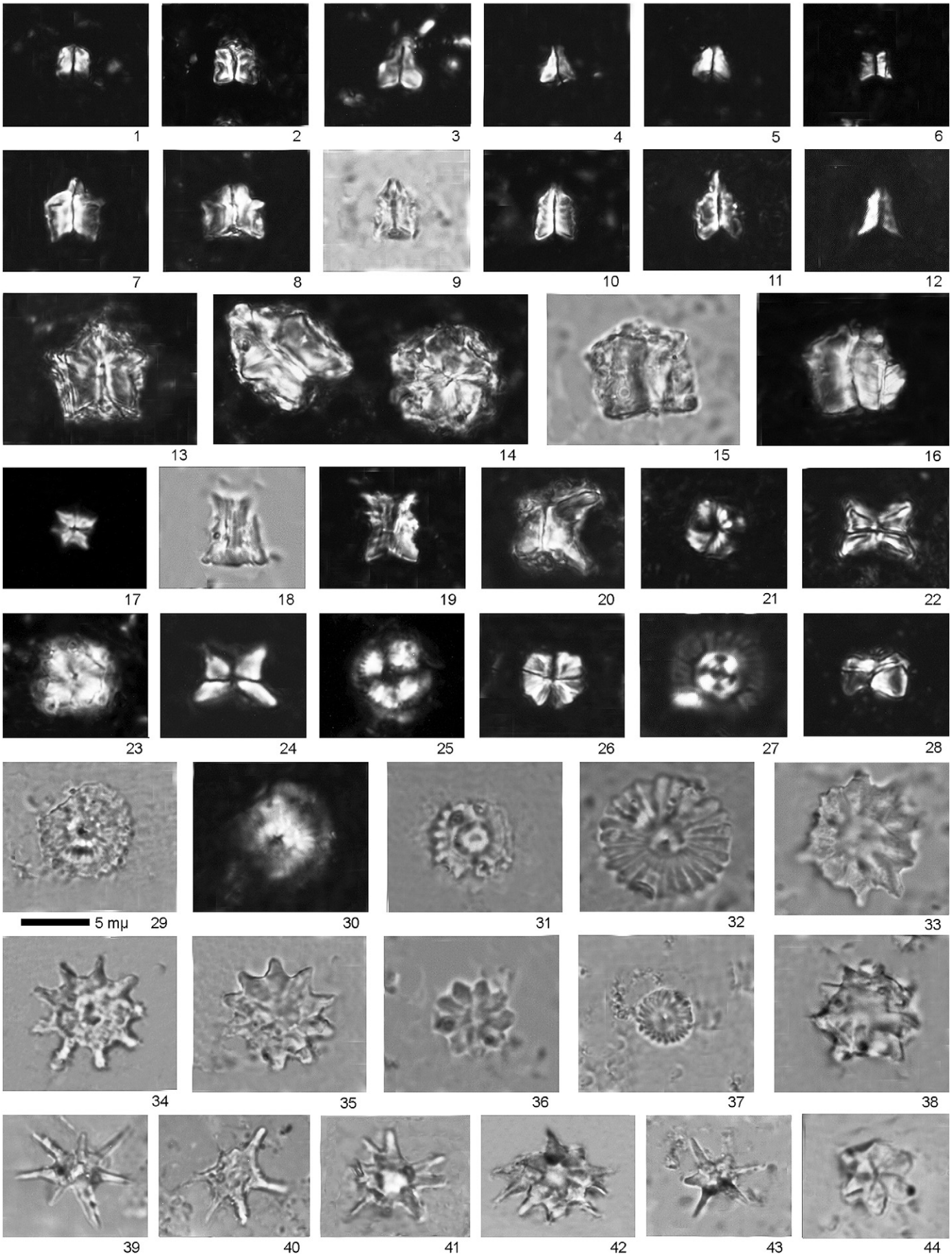
1
2
3
4
5
6
7
8
9
10
11
12
13
14
15
16
17
18
19
20
21
22
23
24
25
26
27
28
5 mμ
29
30
31
32
33
34
35
36
37
38
39
40
41
42
43
44

termination, successively disappear toward the top of the Nalchik Formation and nannofossils become eliminated in the overlying siliceous sediments of the Abazinsk Formation.

4.3.2. Variations in nannofossil assemblages

The following nannofossil taxa can be used as environmental proxies:

1) *Discoaster* — warm-water species which was recently suggested to have oligotrophic affinity (e.g., Hay, 1970; Aubry, 1992; Brallower, 2002), but *D. anartios* only is considered rather as adapted to meso- to eutrophic conditions (Self-Trail et al., 2012);
2) *Sphenolithus* — warm-water oligotrophic species (Bukry, 1981; Brallower, 2002);
3) *Coccolithus* — cosmopolitan species;
4) *Toweius* — meso-eutrophic species, differently interpreted as having cool-water (Aubry, 1992; Brallower, 2002) or cosmopolitian (Kelly et al., 1996; Gibbs et al., 2012) affinity; some species (*T. serotinus*, *T. callosus*, *T. occultatus*) are shown to be adapted to warm-water conditions (Self-Trail et al., 2012);
5) *Fasciculithus* — likely warm-water oligotrophic species (Brallower, 2002);
6) *Thoracosphaera* — stress indicators when occurred in high abundance;
7) *Rhomboaster* — an "excursion taxon", adapted to special PETM conditions.

The ratios and total abundances of nannofossil taxa vary widely across the Paleocene/Eocene transition (see Fig. 8), and "excursion taxa" become more common toward the top of the SBD. The nannofossil assemblage of the sediments underlying the SBD is characterized by high percentages of *Fasciculithus*, *Toweius*, and *Discoaster*, while *Chiasmolithus* is rare (not more than 1–3%) and *Coccolithus* does not exceed 17%. In the pre-SBD record, a progressive increase in the warm-water taxa *Discoaster* and *Sphenolithus* coincides with a negative trend in $\delta^{18}O$, suggesting gradual warming prior to the onset of the PETM. Environmental perturbation can be inferred at the level of sample 708, where the $CaCO_3$ content is relatively high (see Fig. 3) due to the enhanced influx of pelitic calcite, while total nannofossil abundance is at its lowest value in the pre-SBD interval. The nannofossil assemblage at this level is characterized by lower abundances of *Discoaster* and *Toweius* and higher abundances of *Fasciculithus* and *Sphenolithus*, possibly indicating relatively lower-nutrient conditions because the last two taxa are suggested to be oligotrophic indicators (Fuqua et al., 2008). *Discoaster* abundance is significantly greater at the level of samples 711 and 712, corresponding to minor negative peaks of $\delta^{18}O$ during the pre-CIE phase, indicating a temperature discontinuity in the basin prior to the dramatic global warming during the PETM.

Nannofossils decline in abundance up to 0 in the clayey layer underlying the SBD (Layer 4) and in the lowermost part of the SBD. Reappearing at 0.10 m above the base of the SBD, they form an assemblage characterized by low abundance, poor preservation, small specimen sizes, and the strong dominance of *Toweius* (mainly warm-water species — *T. serotinus*, *T. callosus* and *T. occultatus*), *Discoaster* and *Fasciculithus*, although the relative abundance of the latter taxa is lower than in the underlying marl of the Layer 3 (Fig. 9). Coccoliths and sphenoliths decline prominently within the SBD. *Discoaster* is dominated by *D. multiradiatus* and, to a lesser extent, by *D. falcatus*, while the "excursion" species *D. araneus*/*D. anartios* are less abundant and do not exceed one-third of the total *Discoaster* abundance within the SBD.

Plate I. Light microscope images of nannofossils from the Paleocene/Eocene transition in the Kheu section.

1. *Fasciculithus tympaniformis* Hay & Mohler *in* Hay et al., Sample 701, XPL;
2. *F. involutus* Bramlette & Sullivan, Sample 701, XPL;
3. *F. lillianae* Perch-Nielsen, Sample 708, XPL;
4. *F. alanii* Perch-Nielsen, Sample 702, XPL;
5. *F. clinatus* Bukry, Sample 705, XPL;
6. *F. lobus* Bown, Sample A8, XPL;
7, 14. *F. richardii* Perch-Nielsen top and side view, Sample 701, XPL;
8. *F. mitreus* Gartner, Sample 702, XPL;
9, 10. *Fasciculithus* sp. 1 (long column and short apical cone), Sample 715: 9 – IIPL, 10 – XPL;
11. *F. schaubii* Hay & Mohler, Sample 711, XPL;
12. *F. thomasii* Perch-Nielsen, Sample 705, XPL;
13. *F. tonii* Perch-Nielsen: 7 – Sample 701, XPL;
15, 16. *Fasciculithus* sp. 2 (large fasciculith body is formed by several well separated elements), Sample 706, XPL;
17. *F. sidereus* Bybell & Self-Trail, Sample C7;
18, 19. *F. fenestrellatus* Bown, Sample 712: 18 – IIPL, 19 – XPL;
20. *Fasciculithus* sp. 3 (both distal and proximal sides are flared), Sample 706, XPL;
21. *Heliolithus universus* Wind & Wise, Sample 718, XPL;
22. *H. univesus* side view, Sample 719, XPL;
23. *H. riedelii* Bramlette & Sullivan, Sample 705, XPL;
24. *H. riedelii* side view, Sample 719, XPL;
25. *H. bukryi* Wei, Sample 716, XPL;
26. *H. aktasii* Varol, Sample 707, XPL;
27. *H. knoxii* Steurbaut, Sample C6, XPL;
28. *Bomolithus* sp. side view, Sample 705, XPL;
29, 30. *B. aquilis* Bown, Sample 713: 24 – IIPL, 25 – XPL;
31. *B. megastypus* (Bramlette & Sullivan) Bown, Sample 719, IIPL;
32. *D. multiradiatus* Tan, Sample 706, IIPL;
33. *D. splendidus* Martini, Sample 713, IIPL;
34. *D. mediosus* Bramlette & Sullivan, Sample 722, IIPL;
35. *D. falcatus* Bramlette & Sullivan, Sample 707, IIPL;
36. *D. mohleri* Bramlette & Percival, Sample 710, IIPL;
37. *D. lenticularis* Bramlette & Sullivan, Sample 702, IIPL;
38. *Discoaster* sp. asymmetric, Sample 703, IIPL;
39. *D. acutus* Bown, Sample C6, IIPL;
40. *D. araneus* Bukry, Sample C6, IIPL;
41. *D.* cf. *anartios* Bybell & Self-Trail, Sample C7, IIPL;
42. *D.* cf. *anartios* Bybell & Self-Trail, Sample C4, IIPL;
43. *D. mahmoudii* Perch-Nielsen, Sample E2, IIPL;
44. *D. backmannii* Agnini et al., Sample D2, XPL.

The two levels of the SBD with the lowest $\delta^{18}O$ values (Bands II and IV, see Fig. 5) exhibit highly specific, oligotaxonic nannofossil assemblages composed mainly of discoasters and the calcareous dinocyst *Thoracosphaera*. Samples C4 and C5 (Band III, 0.31–0.33 cm), located in the middle of the SBD, contain an assemblage of discoasters (55 and 66% in samples C4 and C5, respectively, among which 14 and 8% are "excursion discoasters"), *Thoracosphaera* (20 and 22%), and *Fasciculithus* (4 and 9%); *Coccolithus* and *Toweius*, which are common and even abun-

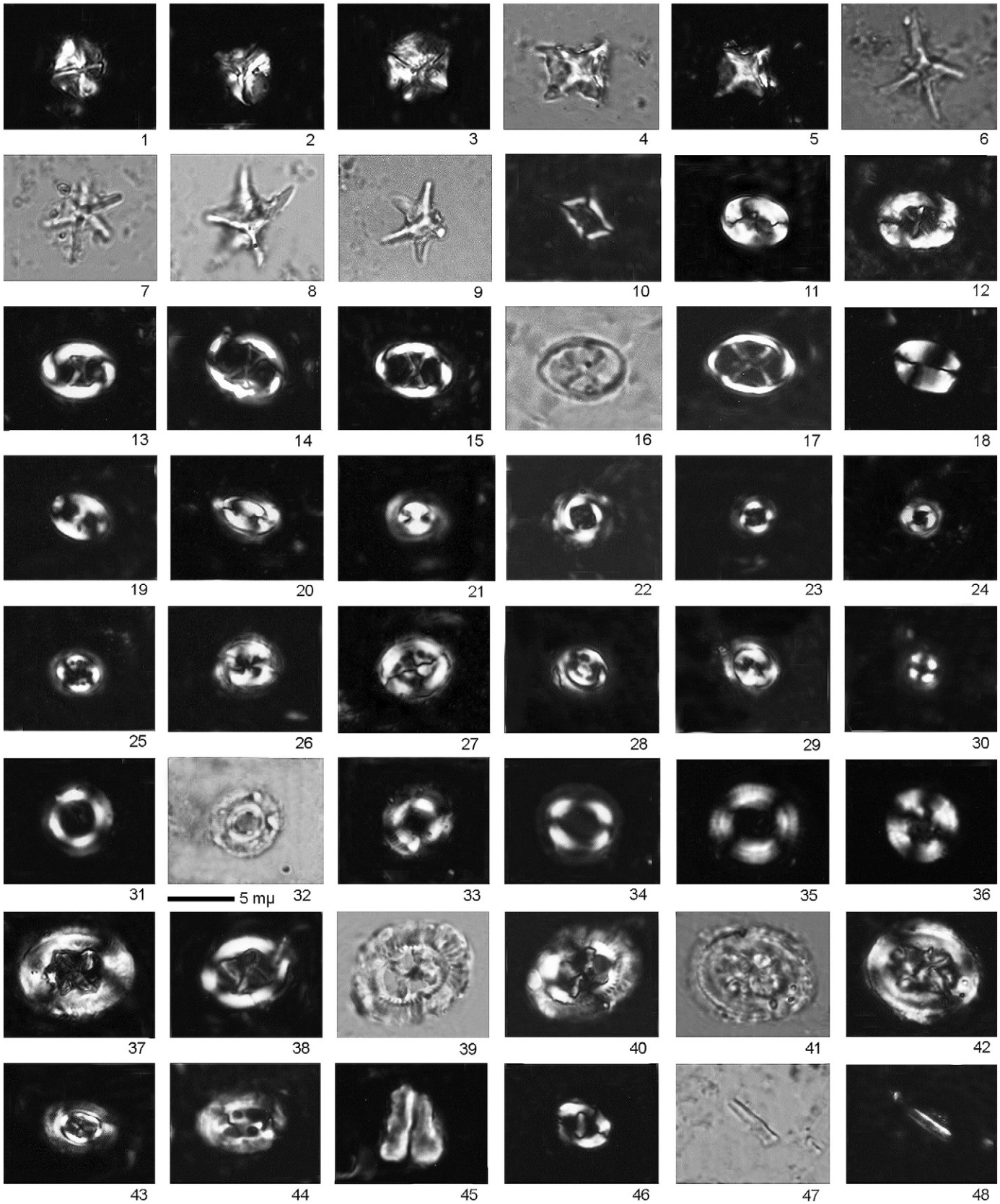

dant in the surrounding sediments, are absent from these samples. Sample D2b from the upper part of the SBD (Band IV, 43 cm) contains a low-abundance assemblage composed of *Thoracosphaera* (46%) and *Discoaster* (43%, among which 16% are "excursion discoasters").

Increased discoaster abundance under more eutrophic conditions in the basin during the SBD accumulation is evident not only in the Kheu section but in all sections studied in the north-eastern Peri-Tethys (Gavrilov et al., 2003). Thus, discoasters thrived when the basin was the most eutrophic. During the late Paleocene and Eocene time, discoasters show inversed correlation with another warm-water taxon, *Sphenolithus* (E.S., personal data), which is believed to indicate oligotrophic conditions. Discoasters were long considered to be warm-water organisms (Bukry, 1971), but later authors suggested that they were oligotrophic species (Aubry, 1998; Brallower, 2002). The wide occurrence of discoasters within the SBD contradicts this hypothesis and rather supports their eutrophic affinity. The adaptation of asymmetric discoasters (*D. araneus* and *D. anartios*) to eutrophic environment was recently suggested by Self-Trail et al. (2012), but our observation on discoaster distribution in the highly fertilized medium, which existed during the SBD accumulation, shows that many rosette-shaped discoasterids thrive under higher nutrient conditions while other nannofossil taxa become significantly oppressed. Their positive correlation with stress taxon *Thoracosphaera* within the SBD and inversed correlation with *Coccolithus* and *Toweius* support the better adaptation of discoasters to abnormal conditions. At the same time, temperature control seems to be more important factor for discoaster distribution than nutrient availability.

The "excursion taxa" *Rhomboaster* and asymmetric *Discoaster* remain common in the short interval above the SBD (samples 715 and 716, from 0.60 to 0.78 cm), whereas the discoaster abundance significantly decreases. The assemblage from the later phase of the CIE is characterized by the wide domination of *Coccolithus* and *Toweius*, while *Fasciculithus* and *Rhomboaster* reduce their abundance (see Fig. 9). This likely indicates the beginning of environmental restoration.

In the CIE recovery phase, the nannofossil assemblages restore their pre-PETM ratios and abundance, but *Fasciculithus* progressively decline during the later stage of the CIE recovery. High abundance of *Toweius* is related to income of long-lived species *T. callosus*, which remains abundant during early Eocene. The decline of nannofossils at ~4 m above the SBD corresponds to a notable facies change related to enhanced siliciclastic discharge, probably caused the bloom of siliceous microplankton and collapse of calcareous microbiota.

4.3.3. Preservation and size

The low abundance of nannofossils within the SBD may be due to both low primary productivity and enhanced dissolution under high-CO_2 conditions in TOC-rich sediments. To evaluate the possible effect of selective dissolution on the taxonomic composition of the nannofossil assemblages, we estimated the total amounts of the most and least dissolution-resistant nannofossil taxa at selected levels of the SBD. Empirical studies of the susceptibility of Cenozoic nannofossils to dissolution (Bukry, 1981) indicate that discoasters and coccoliths are the most resistant taxa, while *Transversopontis* (*Pontosphaera*) is the most sensitive to dissolution. Under stronger dissolution, $CaCO_3$, total nannofossil abundance and relative abundance of the most susceptible species will significantly decrease and the amount of discoasters will increase in relative abundance. Episodes of enhanced dissolution are likely to correspond to the highest TOC levels due to the high pCO_2 under redox conditions. However, the abundances of *Discoaster* and *Pontosphaera pulchra* in several SBD samples are not directly correlated

Plate II. Light microscope images of the nannofossils from the Paleocene/Eocene transition in the Kheu section.

1, 2. *Rhomboaster intermedia* Romein, XPL: 1 — Sample 706, 2 — Sample 709;
3, 4, 5. *R. cuspis* Bramlette & Sullivan: 3 — Sample 710, XPL, 4 — Sample C6, IIPL, 5 — Sample C6, XPL;
6, 7. *R. calcitrapa* Gartner: 6 — Sample A7, 7 — Sample D4, IIPL;
8. *Rhomboaster spineus* (Shafik & Stradner) Perch-Nielsen, Sample D4, IIPL;
9. *Tribrachiatus* cf. *bramlettei* Brönnimann & Stradner, Sample D4, IIPL;
10. *Scapholithus apertus* Hay & Mohler, Sample 703, XPL;
11–13. Three specimens of *Neochiastozygus distentus* (Bramlette & Sullivan) Perch-Nielsen, showing progressive decrease in calcification, XPL: 11 — Sample 701, 12 — Sample 710, 13 — Sample A8a;
14. *N. junctus* (Bramlette & Sullivan) Perch-Nielsen , Sample A7, XPL;
15. *N. concinnus* (Martini) Perch-Nielsen, Sample A7, XPL;
16–17. *N. chiastus* (Bramlette & Sullivan) Perch-Nielsen, Sample 721: 16 — IIPL, 17 — XPL;
18. *Pontosphaera plana* (Bramlette & Sullivan) Haq, Sample 718, XPL;
19. *P. pulchra* (Deflandre in Deflandre & Fert) Romein, Sample B1, XPL;
20. *Prinsius bisulcus* (Stradner) Hay & Mohler, Sample 700, XPL;
21. *P. martini* (Perch-Nielsen) Haq, Sample D3, XPL;
22. *T. callosus* Perch-Nielsen, Sample 702, XPL;
23. *T. pertusus* (Sullivan) Romein, Sample 703, XPL;
24. *T. rotundus* Perch-Nielsen, Sample 700, XPL;
25. *T. serotinus* Bybell & Self-Trail, Sample 718;
26. *T. eminens* (Bramlette & Sullivan) Perch-Nielsen, Sample 707
27, 28. *T. tovae* Perch-Nielsen, XPL: 27 — Sample 706, 28 — Sample 702;
29. *T. occultatus* (Locker) Perch-Nielsen, Sample 701, XPL;
30. *Coccolithus pauxillus* Bown, Sample A8a, XPL;
31. *C. bownii* Jiang and Wise, Sample 706, XPL;
32, 33. *C. foraminis* Bown, Sample 705: 32 — IIPL, 33 — XPL;
34. *C. latus Bown*, Sample D3, XPL;
35. *Ericsonia robusta* (Bramlette & Sullivan) Edwards & Perch-Nielsen, Sample C1, XPL;
36. *E. subpertusa* Hay & Mohler, Sample 705, XPL;
37. *Chiasmolithus bidens* (Bramlette & Sullivan) Hay & Mohler, Sample 702, XPL;
38. *C. edentulus* Heck and Prins, Sample 700, XPL;
39, 40. *C. consuetus* (Bramlette & Sullivan) Hay & Mohler, Sample 705: 39 — IIPL, 40 — XPL;
41, 42. *Chiasmolithus sp.*, Sample 701: 41 — IIPL, 42 — XPL;
43. *Campylosphaera eodela* Bukry & Percival, Sample A7;
44. *Ellipsolithus distichus* (Bramlette & Sullivan) Sullivan, Sample 702, XPL;
45. *Zygrhablitgus bijugatus* (Deflandre in Deflandre and Fert) Deflandre, Sample 710, XPL;
46. *Zygodiscus herlyni* Sullivan, Sample 711, XPL;
47, 48. *Blackites solus* Perch-Nielsen, Sample A7: 47 — IIPL, 48 — XPL.

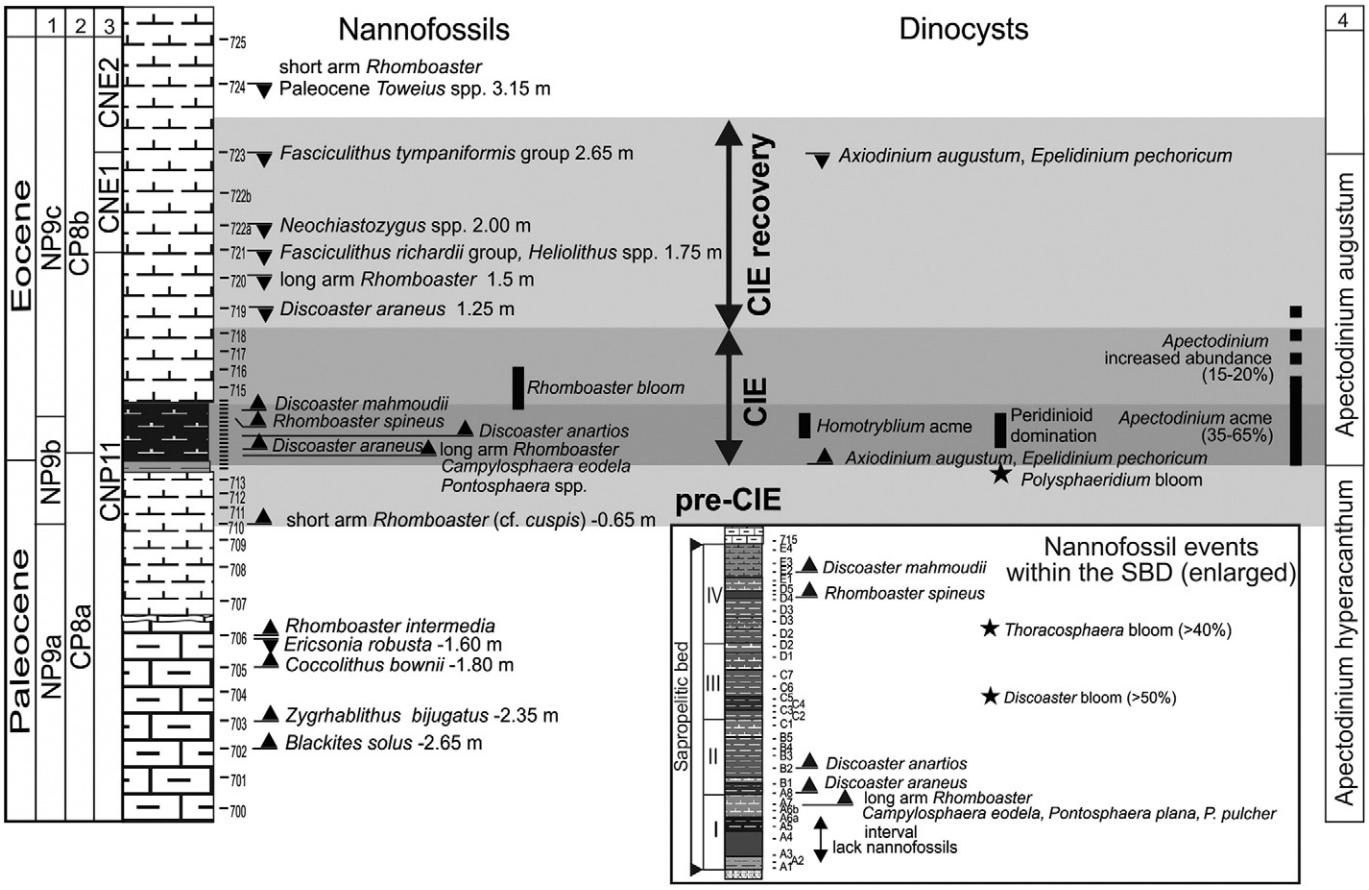

Fig. 7. Nannofossil and dinocyst events across the Paleocene/Eocene transition in the Kheu section. The inset in the lower part of the figure shows enlarged picture of the SBD. 1 — nannofossil zonation of Martini (1971), 2 — nannofossil zonation of Okada and Bukry (1981), 3 — nannofossil zonation of Agnini et al. (2014), and 4 — dinocyst zonation of Powell (1992).

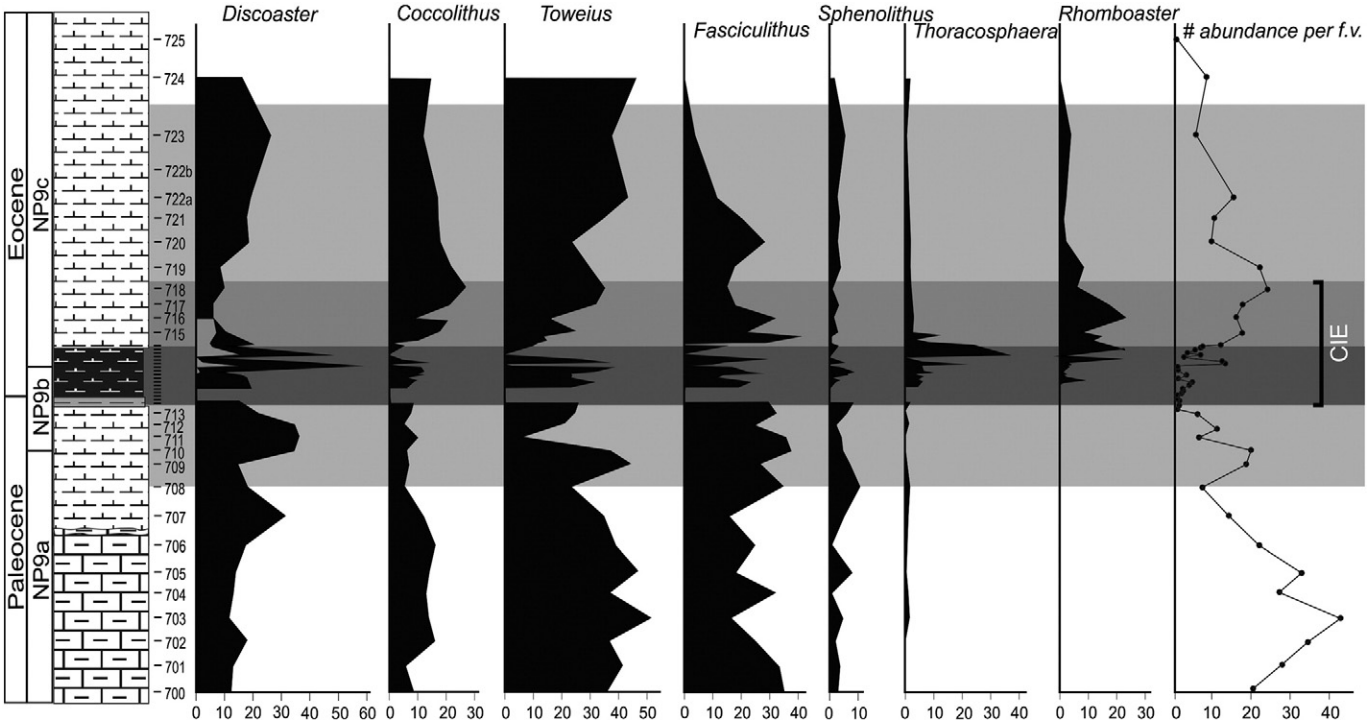

Fig. 8. Ratios of the major nannofossil taxa across the Paleocene/Eocene transition and average nannofossil abundances per microscope field of view caunted from 50 f.v. The grey insert in the *Discoaster* curve represents the percentage of "excursion" discoasters (*D. anartios*/*D. araneus*).

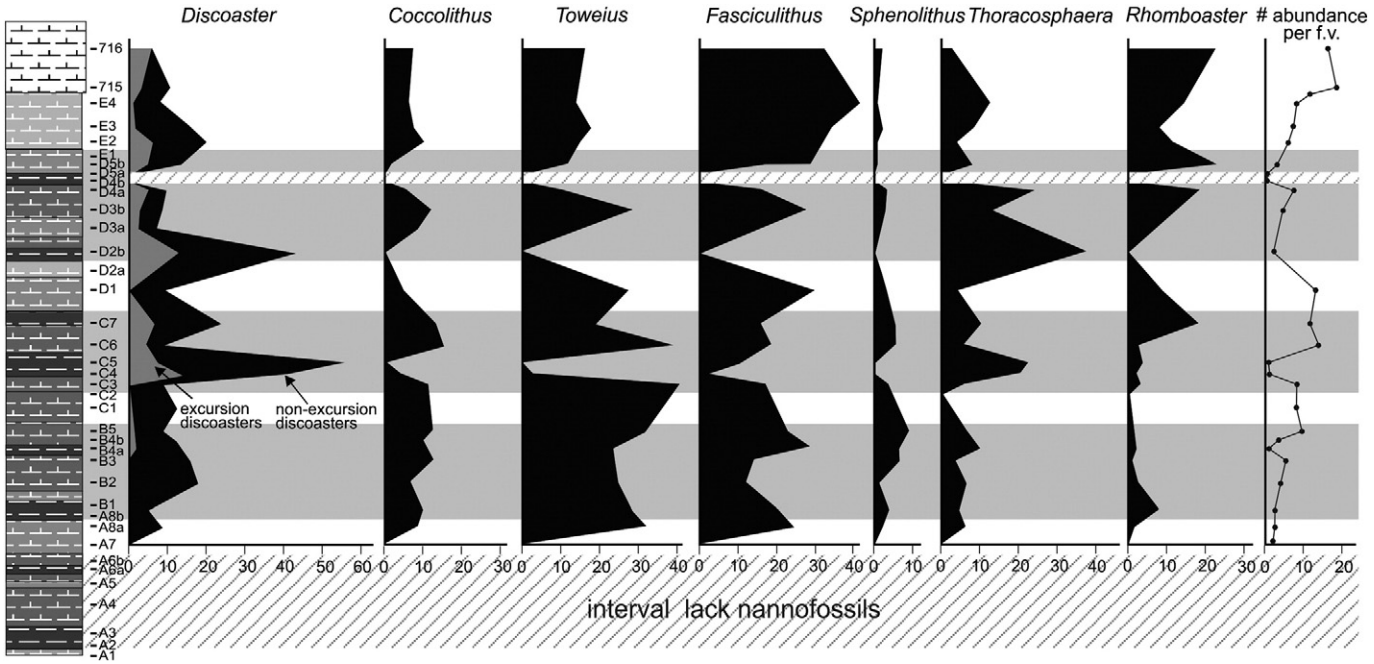

Fig. 9. Ratios of the major nannofossil taxa and average nannofossil abundances within the SBD.

with TOC, $CaCO_3$ or total nannofossil abundance (Table 1). The relatively high abundance of *Pontosphaera pulchra* and higher $CaCO_3$ content of the low-abundance assemblage in the lower part of the SBD (samples A7 and A8a) indicate a weak dissolution effect. Thus, the low species diversity in the most enriched in TOC interval is probably due to ecological limitation. The poor preservation of nannofossils within the SBD is more likely caused by weak coccolith and nannolith calcification under unfavourable PH-conditions. The most specimens, especially discoasters, are very thin and appeared broken, but not strongly dissolved.

The nannofossils found in the CIE interval (including the SBD, the main body of CIE and its recovery) are mostly small in size, that may indicate eutrophic conditions (Lees et al., 2005) or a response of coccolithophores to increased *p*CO2 and related problem with calcification (Erba et al., 2010). Both "excursion" (*D. anartios*/*D. araneus*) and "non-excursion" discoasters (*D. falcatus*, *D. multiradiatus*, *D. salisburgensis*) exhibit malformation within the SBD. Notably, numerous malformed discoasters (mostly *D. falcatus*) are present in the sediments underlying the SBD. Other heavily calcified nannoliths (fasciculiths and helioliths) and coccoliths also show malformation during the accumulation of TOC-rich sediments. The reduced $CaCO_3$ production and malformation indicate that the living organisms suffered from poor biocalcification in the basin, probably due to elevated pCO_2 levels (Riebesell et al., 2000). Calcium carbonate deficiency might explain the lower abundance or even absence of heavily calcified coccoliths at some levels of the SBD. At the same time, it should be emphasized, that even heavily calcified fasciculiths (*F. schaubii*, *F. thomasii*, a.o.), reoccurred during the CIE recovery, are characterized by much smaller, than pre-PETM size.

Table 1
Correlations between the TOC and $CaCO_3$ values and the most dissolution-resistant (*Discoaster*) and susceptible (*Pontosphaera*) taxa at selected levels of the SBD.

Sample no.	Pontosphaera n/m^2	Discoasters n/m^2	TOC,%	$CaCO_3$,%	# nannofossil abundance per f.w.
D2b	–	24.1	5.15	9.7	2.5
C7	–	26.4	3.51	6.9	12.1
C5	–	28.2	4.20	6.8	0.2
C4	–	34.7	4.80	9.7	1.2
A8a	5.6	19.0	1.47	16.0	3.8
A7	6.5	10.23	2.01	13.3	3.1

4.4. Palynology

Most of the palynological samples from the Paleocene/Eocene transition in the Kheu section (except for the samples 700 and 708) contain abundant and diverse palynological assemblages, and all of them contain dinoflagellate cysts (Figs. 10, 11, Plate III).

Dinocyst paleoenvironmental reconstructions were based on several studies (Brinkhuis, 1994; Powell et al., 1996; Sluijs et al., 2005: Crouch and Brinkhuis, 2005), and we followed the approach of Sluijs and Brinkhuis (2009) in using a largely empirically based grouping of morphologically similar forms. We recognized the following groups of dinocyst taxa:

1. *Apectodinium* spp. and *Epelidinium pechoricum* (wetzelielloids) are interpreted as heterotrophic dinoflagellates that fed on other plankton, are thought to be related to globally high SSTs and high nutrient availability, and are typical of coastal and neritic settings;
2. Deflandroids (*Deflandrea*, *Alterbidinium*, *Senegalinium*, *Lentinia*) are interpreted as heterotrophic dinoflagellates, are thought to be related to enhanced coastal and neritic productivity in well-mixed (unstratified) waters, and are typical of coastal and brackish settings and tolerant of low salinity;
3. *Phthanoperidinium* spp. are possibly heterotrophic dinoflagellates, are indicators of high productivity in shallow marine settings, and are tolerant of low salinity;
4. *Kenleyia*-complex species (*Kenleyia*, *Muratodinium fimbriatum*, *Cordosphaeridium*, *Fibrocysta*) are probably autotrophic dinoflagellates, are typical of coastal and neritic environments, and are thought to indicate warm SSTs;
5. *Areoligera*-complex species (*Areoligera*, *Glaphyrocysta*, *Adnatosphaeridium*) are interpreted as autotrophic dinoflagellates,

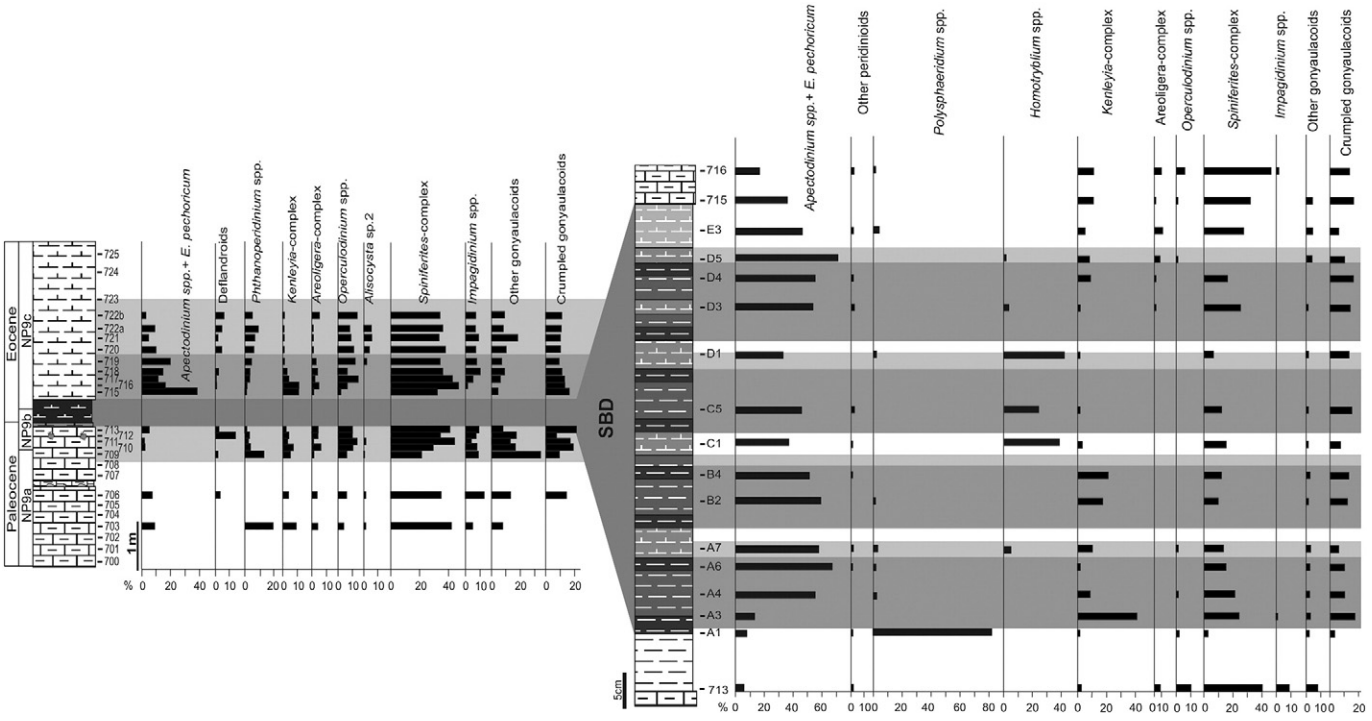

Fig. 10. Quantitative distribution of dinocyst eco-groups across the Paleocene/Eocene transition and the SBD in the Kheu section.

are typical of high-energy inner-neritic settings, and are abundant during transgressive trends;

6. *Operculodinium* spp. are interpreted as autotrophic dinoflagellates and are typical of open-marine and inner-neritic environments;
7. *Alisocysta* sp. 2 sensu Heilmann-Clausen is of unknown palaeoecological affinity;
8. *Polysphaeridium* spp. are autotrophic dinoflagellates whose modern representatives are typical of low-latitude hyposaline or hypersaline lagoon settings;
9. *Homotryblium* spp. are interpreted as autotrophic dinoflagellates and are most typical of restricted marine to inner-neritic hypersaline environments;

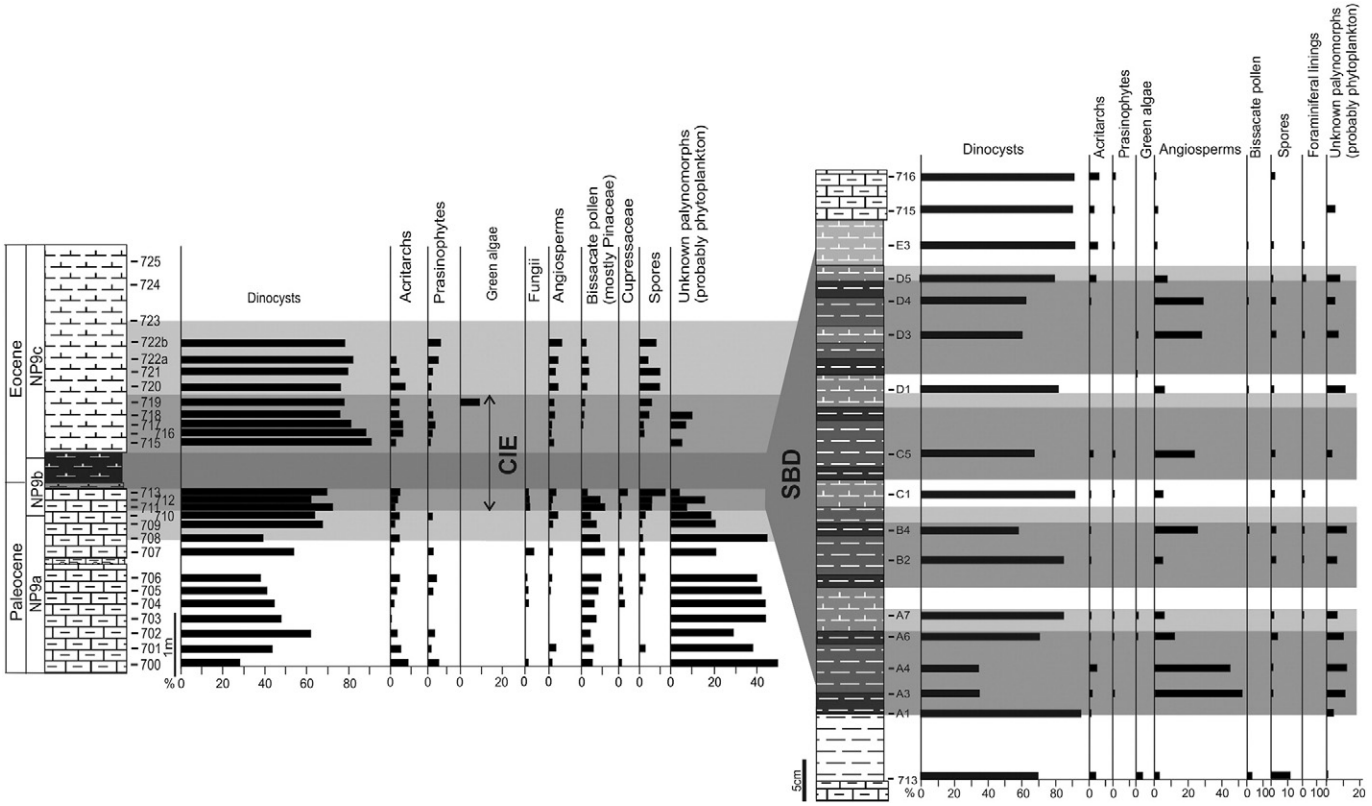

Fig. 11. Quantitative distribution of palynomorph groups across the Paleocene/Eocene transition and the SBD in the Kheu section.

10. *Spiniferites*-complex species (*Spiniferites*, *Achomosphaera*, *Spiniferella*, *Rottnestia*) are interpreted as normal marine autotrophic dinoflagellates, found from inner-neritic to oceanic settings, and their abundances are associated with transgressive trends;
11. *Impagidinium* spp. are interpreted as outer-neritic to oceanic species, and an increase in their abundance indicates a sea level rise;
12. Other gonyaulacoids (mostly gonyodomids).

The greenish marl that underlies the SBD (samples 703–713) is characterized by the presence of *Apectodinium* species (*A. homomorphum*, *A. quinquelatum* and *A. hyperacanthum*) and is attributed to the interval of the NW European dinocyst zone D5a (Luterbacher et al., 2004) and the *A. hyperacanthum* zone of Powell (1992).

The palynological assemblages of this part of the section are relatively rich in palynomorphs and are dominated by either dinocysts (30–70%) or green algae (up to 50%); bisaccate pollen grains represent up to 10% of the assemblage (Figs. 10 and 11). The dinocysts found in this interval are mostly gonyaulacoids (up to 95%); *Apectodinium* does not exceed 10% and represents only 5% at the level just below the CIE. The dinocyst assemblage from samples 703–713 is dominated by the *Spiniferites* complex and contains *Impagidinium* spp. (up to 10%), indicating neritic marine environments and probably a relative sea-level rise.

The PETM interval is characterized by the occurrence (sample A1) of the key dinocyst species *Axiodinium* (previously *Apectodinium*) *augustum* and *Epelidinium pechoricum*, suggesting that it corresponds to the *Apectodinium augustum* zone of Powell (1992). The palynomorph assemblages within the SBD (samples A1–E3) are dominated by dinocysts, with reduced amounts of other algae and relatively abundant angiosperm pollen. The dinocyst assemblages are characterized by a general change in the gonyaulacoid/peridinioid ratio: peridinioids (represented only by wetzelielloids) become abundant within the SBD, indicating drastic environmental changes during the PETM. In the lowermost part of the SBD (sample A1), the dinocyst assemblage is marked by a strong influx (80%) of *Polysphaeridium subtile*, possibly indicating an extreme environmental perturbation at the onset of the CIE and even the occurrence of high-salinity lagoon settings. The peak abundance of *P. subtile* is followed at the next level (sample A3) by a relatively high abundance of the *Kenleyia* complex and a slight influx of *Spiniferites* complex, which are interpreted as evidence of a low transgressive pulse or, alternatively, of a salinity change. *Apectodinium* spp. then become dominant in samples A4–B4, suggesting enhanced nutrient availability during the CIE. In the middle part of the SBD (samples C1–D3), *Homotryblium* spp. replace *Apectodinium* as the dominant group, probably indicating an environmental perturbation involving a change in nutrient availability. In the upper part of the SBD, *Apectodinium* again exceeds 70% of the assemblage, while the *Spiniferites* complex increases slightly in the uppermost portion of the SBD (sample E3). In general, the dinocyst assemblages within the SBD show a near-absence of *Impagidinium* spp. and a decrease in deflandroids and *Phthanoperidinium* spp.

In the sediments overlying the SBD, which correspond to the later stages of the CIE (NP9c subzone), *Ax. augustum* and *E. pechoricum* remain present. The palynomorph assemblages of this interval are dominated by dinocysts with rare acritarchs, prasinophytes and terrestrial spores and show reduced angiosperm abundance (see Fig. 11). The dinoflagellate assemblages again show a general dominance of gonyaulacoids and a gradual decline in *Apectodinium* abundance (from 40% to 5%). Members of the *Spiniferites* complex are generally abundant, and *Impagidinium* spp. re-occur in the assemblage. Among peridinioids, deflandroid taxa and *Phthanoperidinium* spp. become more abundant again; at the same time, the gonyaulacoids *Operculodinium* spp., *Alisocysta* and the *Areoligera* complex become newly abundant, indicating the restoration of the pre-PETM marine environment.

5. Discussion

Our multidisciplinary study of the PETM record in the Kheu section reveals intricate relationships among the biotic, sedimentological and geochemical phenomena involved in this critical palaeoecological event. Both geochemical and paleontological results show the rapid, dramatic development of ecological stress in the basin at the onset of the PETM. At the same time, this critical global event was preceded by apparently simultaneous changes in $\delta^{13}C$ and $\delta^{18}O$, $CaCO_3$ and the abundances and taxonomic compositions of nannofossil and dinocyst assemblages during the pre-CIE phase. The general succession of biotic and abiotic events at the Paleocene/Eocene transition is shown in Fig. 12.

The progressive decrease in total nannofossil abundance and the related drop in $CaCO_3$ content in the sediments underlying the SBD (samples 700–709), coinciding with the reduced abundance of *Spiniferites*-complex dinocysts in the same interval suggest a regressive trend, accompanied by a slight warming, as indicated by the gradual decrease in $\delta^{18}O$ and increase in relative abundance of warm-water discoasters. The palaeoenvironmental trends corresponding to the pre-CIE interval of minor carbon and oxygen isotope variations are poorly understood due to the conflicting geochemical and palaeontological results. The level of sample 710 (−0.65 m) is marked by a small positive peak in $\delta^{13}C$ corresponding to relatively higher $CaCO_3$ content, increased nannofossil abundance, domination of dinocysts over other palynomorphs and a slight increase in *Spiniferites*-complex in dinocyst assemblage. All these, possibly, indicate a short transgressive pulse. A small positive $\delta^{18}O$ peak at this level, which suggests relative cooling, corresponds, nevertheless, to a significant increase in the warm-water *Discoaster*. Nannofossils tend to decline above this level in the upper part of Layer 3 (samples 711–712; see Fig. 8) and became absent in the Layer 4 that implies the beginning and progressive development of unfavourable conditions for the nannoplankton community. The dinocysts become more abundant in this interval, especially the *Spiniferites*-complex. Together, these signal the onset of initial, albeit not very strong, environmental perturbations.

The pre-PETM environmental perturbations evidenced in the north Caucasian basin are not the unique phenomena. A similar prelude to the main CIE in form of small-scale $\delta^{13}C$ shifts can be seen in shelves and oceanic areas (e.g., Gangyi Lu et al., 1996; Bains et al., 1999; Tipple et al., 2011; Self-Trail et al., 2012; Manners et al., 2013; Giusberti et al., 2015), as well as in continents (Smith et al., 2007; Bowen et al., 2014). At the same time, very gradual decrease in $\delta^{13}C$ preceded to the CIE is documented in the southern Tethyan margin (Khozyem et al., 2014, 2015). Negative trends in $\delta^{18}O$ prior to the onset of PETM detected in both oceanic (Thomas et al., 2002) and continental (Secord et al., 2010) settings suggest initial warming preceded the main dramatic environmental changes.

The SBD accumulation is evidently caused by greatly enhanced supply of nutrients, which stimulated a burst of productivity in the basin. Such increased fertilization of the basin could be induced by upwelling (which would not function effectively in this large, shallow basin) or by an enhanced nutrient supply from the land. The latter and most probable triggering process could be initiated by a rapid sea-level change. Dramatic sea-level fall prior to PETM detected in many World areas (Gavrilov et al., 1997; Speijer and Wagner, 2002; Sluijs et al., 2008; Egger et al., 2009, a.o.) might have the magnitude at least 20 m (Speijer and Wagner, 2002; Pujalte et al., 2014) and evidently corresponds to eustatic sea-level fall in the middle of TA2 cycle (Haq et al., 1987). In some sections of NE Peri-Tethys, the SBD onlaps underlying sediments with sharp erosional surface and long-ranging hiatus (e.g., Aktumsuk section, western Aral Lake, where the SBD onlaps Campanian sediments); in some other localities, the SBD overlays the layer with rounded pebble composed of the lower Paleocene marl (e.g., Dzhengutay section, eastern Caucasus). The rapid regression led to the long-distant seaward displacement of the shoreline in the wide epeiric Peri-Tethyan basin and the occurrence of ephemeral lagoons

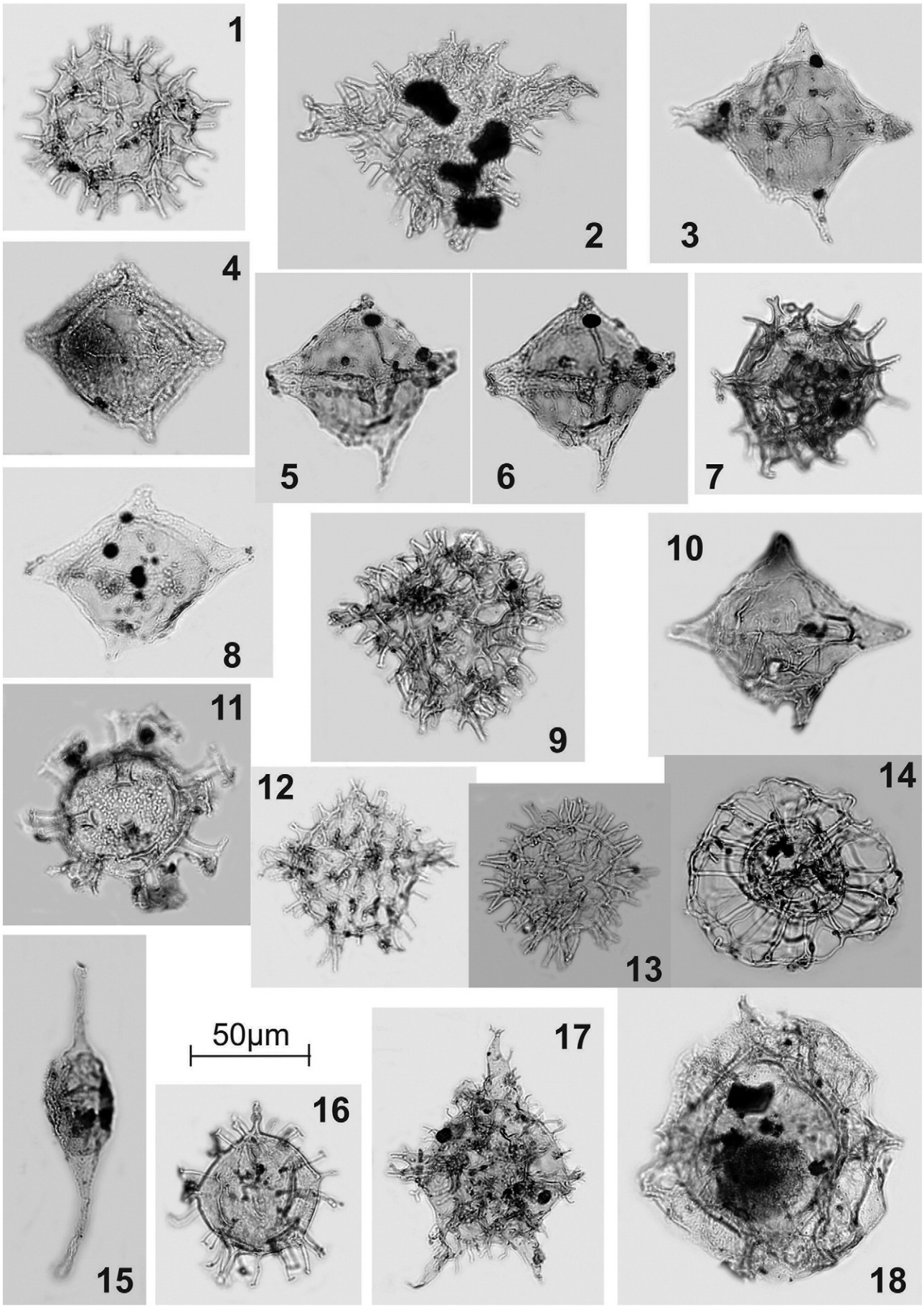
1
2
3
4
5
6
7
8
9
10
11
12
13
14
15
50μm
16
17
18

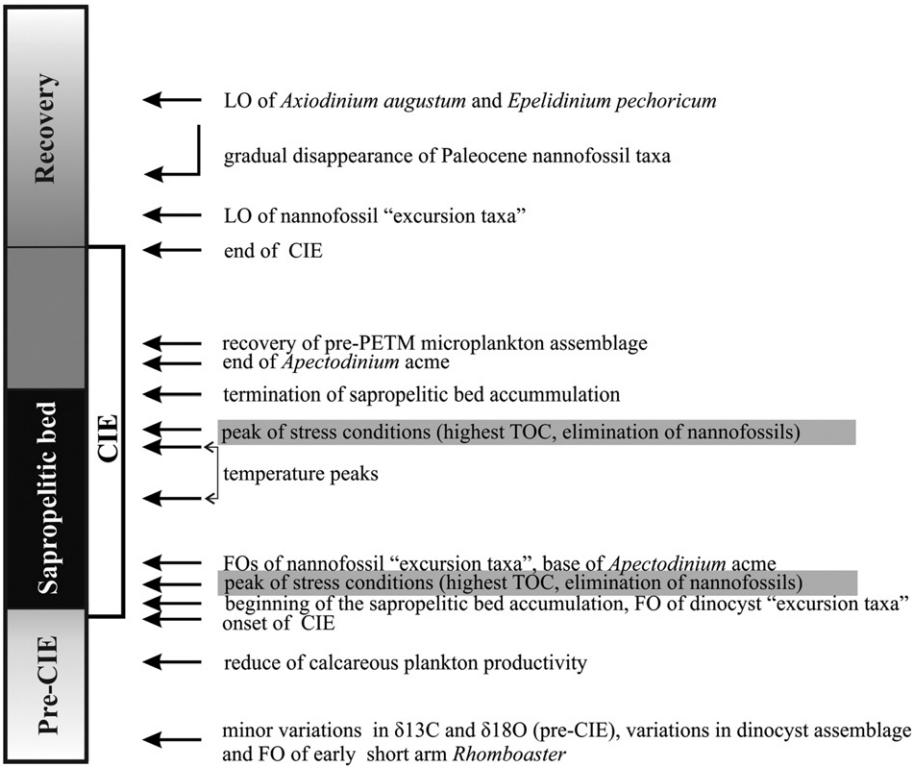

Fig. 12. Microplanktonic and geochemical events documented in the PETM record of the Kheu section.

and wetlands in the emerged territories. Thus, the drastic facies change prior to the SBD accumulation, which led to the formation of non-calcareous clay (Layer 4), was evidently caused by sea-level fall and shoaling of the basin, leading to the decline of nannofossils and dinocysts. The onset of the SBD accumulation over wide territory (more than 2500 km, from Crimea to Central Asia) was related to subsequent rapid large-scale transgression and drowning of the wetlands formed during preceded short-lived sea-level fall, where high concentrations of nutrients accumulated (Gavrilov et al., 2003).

The base of the SBD (sample A1, 0 m) is marked by a very short bloom of gonyaulacoid species *Polysphaeridium subtile*. *P. subtile* represents a resting cyst of an extant species *Pyrodinium bahamense* – a photoautotrophic dinoflagellate existing at the present time in shallow tropical marine and estuary systems and which occurs in bloom in very narrow inlets with low tidal variation, surrounded by mangrove swamps (Hereid, 2007). According to Reinchart et al. (2004), high abundance of *Polysphaeridium* may be explained by the establishment of seasonal hyperstratification with hypersaline surface waters. These also evidence the formation of non-calcareous clay (Layer 4, prior to SBD) during sea-level fall and likely indicate the occurrence of an ephemeral lagoon with increased salinity at the regressive stage; their flooding during subsequent rapid sea-level rise led to formation of oligotaxonic *Polysphaeridium* dinocyst assemblage and, possibly, caused water column stratification during initial stages of the SBD accumulation.

It is widely considered that the presumably heterotrophic dinoflagellate genus *Apectodinium* (originated close to the Danian-Selandian boundary in low latitudes, Brinkhuis, 1994) become abundant in mid- and high latitudes toward the beginning of the PETM (Crouch et al., 2001, 2003; Sluijs et al., 2006, 2007, 2010; Sluijs and Brinkhuis, 2009). In the Kheu section, however, the first acme of *Apectodinium* spp. occurs

Plate III. Light microscope images of the dinocysts from the Paleocene/Eocene transition in the Kheu section.

1 — *Apectodinium homomorphum*; sample 715, slide 715-1;
2 — *Axiodinium* (=*Apectodinium*) *augustum*; sample 721, slide 721-1;
3 — *Epelidinium* (=*Wilsonidium*) *pechoricum*; sample A1, slide A1-1;
4 — *Epelidinium* (=*Wilsonidium*) *pechoricum*; sample 721, slide 721-1;
5, 6 — *Epelidinium* (=*Wilsonidium*) *pechoricum*; sample A1, slide A1-1;
7 — *Apectodinium homomorphum*; sample C1, slide C1-1;
8 — *Epelidinium* (=*Wilsonidium*) *pechoricum*; sample A1, slide A1-1;
9 — *Apecotidinium quinquelatum*; sample A1, slide A1-1;
10 — *Epelidinium* (=*Wilsonidium*) *pechoricum*; sample A1, slide A1-1;
11 — *Homotryblium tasmaniense*; sample C1, slide C1-1;
12 — *Apecotidinium quinquelatum*; sample A1, slide A1-1;
13 — *Apectodinium homomorphum*; sample 716, slide 716-1;
14 — *Adnatosphaeridium multispinosum*; sample 716, slide 716-1;
15 — *Biconidinium longissimum*; sample 716, slide 716-1;
16 — *Apectodinium homomorphum*; sample D1, slide D1-1;
17 — *Apectodinium parvum*; sample C1, slide C1-1;
18 — *Muratodinium fimbriatum*; sample 716, slide 716-1.

~5 cm above the base of the SBD and the onset of CIE. This bioevent succeeds the bloom of *P. subtile* and corresponds to the level with a largely increased abundance of warm-water gonyaulacoid *Kenleya*-complex and a slight influx of *Spiniferites*-complex; co-occurrence of these taxa and dramatic decrease of $\delta^{18}O$ likely suggests transgressive trend and climatic warming associated with the onset of PETM. *Apectodinium* spp. remains to be abundant throughout the whole CIE interval (30–70%). Two intervals of its highest abundance (sample A6a at 0.09 m and D5a at 0.52 m) coincide with the influx of angiosperm pollen and high TOC values that possibly can be associated to two episodes of relative sea-level rise and related increased nutrient input.

The lower part of the SBD from 0 to ~0.35 m is characterized by highest basinal productivity inferred from high HI. The increased relative abundance of both *Apectodinium*- and *Kenleya*-complexes, although they are inversely correlated within this interval, and poor nannofossil assemblage dominated by small *Toweius* spp. indicate warm eutrophic environment. The change from *Apectodinium*-dominated to *Homotryblium* spp.-dominated dinocyst assemblage (between samples C1 and D1, i.e. from ~0.28 to ~0.58 m) corresponds to increase of terrestrial organic matter influx, reduce of basinal productivity (lower HI) and partial recovery of nannofossil assemblages in the middle of the SBD. More likely, these variations were caused by relative small-scale sea-level fall led to reduce of flooded territories, which served as a source of enhanced nutrient supply, temporal decrease in fertilization and relative weakening of stress conditions that caused the accumulation of the relatively more calcareous and less enriched in TOC middle part of the SBD.

The most specific nannofossil assemblages dominated by warm-water *Discoaster* and stress taxon *Thoracosphaera* are found at the levels of the samples C5 and D2b (~0.33 and 0.43 m, respectively). These specific assemblages correspond to the most negative $\delta^{18}O$ peaks (see Fig. 5) and, evidently, the most dramatic warming episodes during the SBD accumulation oppressed most of the nannofossil taxa.These events seem to be of regional nature, as they do not correspond to significant variations in $\delta^{13}C$.

The upper part of the SBD is characterized by new increase in abundance of *Apectodinium* spp. in the dinocyst assemblage and the beginning of the bloom of "excursion taxon" *Rhomboaster* in the nannofossil

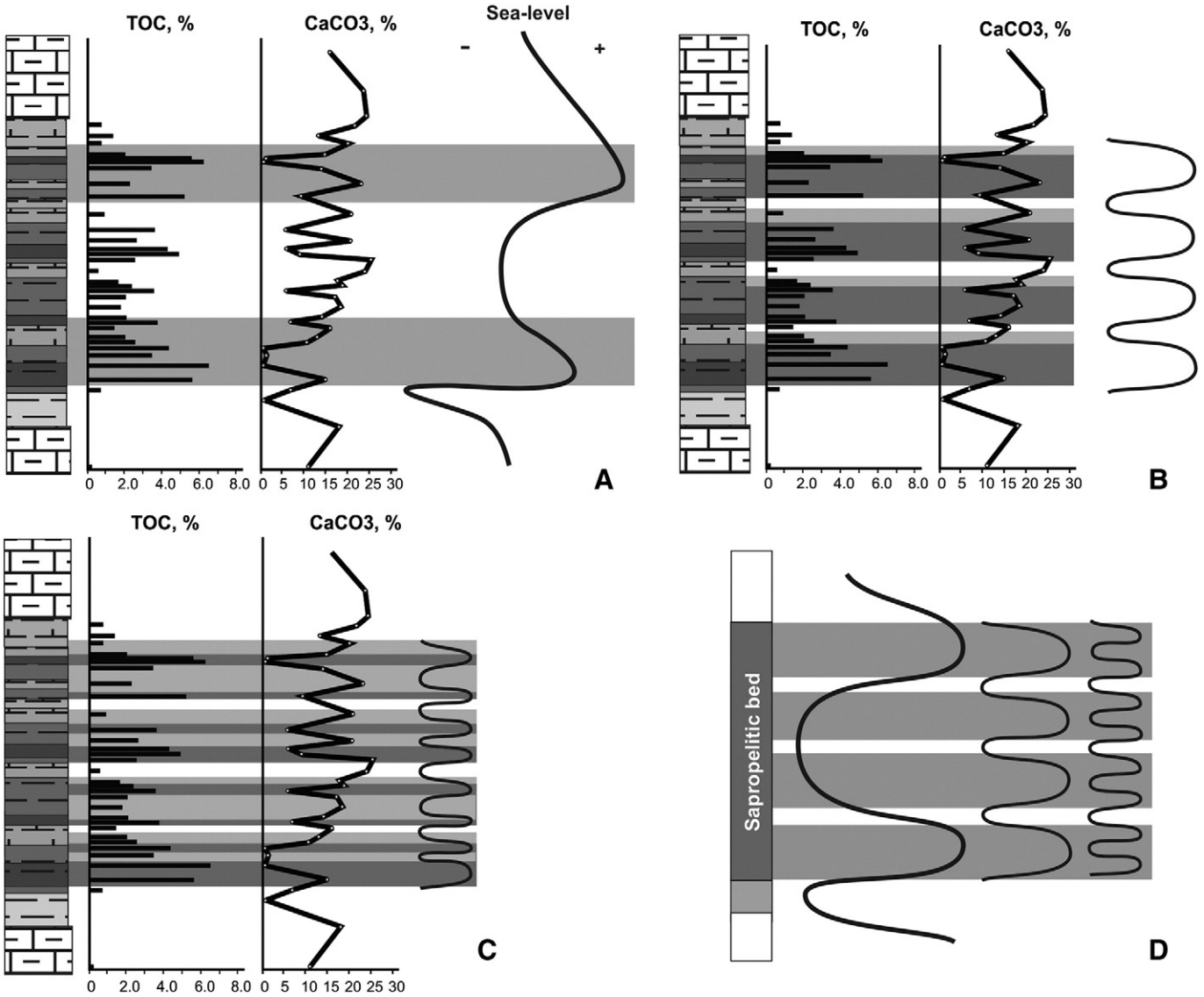

Fig. 13. Various cyclicity detected in the SBD of Kheu section: A — general triple structure of the SBD, more likely related to eustatic sea-level changes, which caused relative weakening of critical conditions during relative sea-level fall corresponding to the middle part of the SBD; B — four bands built up of dark and pale sediments (enriched in organic matter in major and minor extends), which more likely correspond to precession cycles; C — small-scale rhythmicity within the bands, related to minor fluctuations of TOC and $CaCO_3$ concentrations; D — idealized presentation of superimposition of the cycles of different orders.

assemblage. These trends, completed by wide domination of terrestrial organic matter, more likely indicate new sea-level rise, when shoreline moved landward well over its position in the time of precedent transgressive pulse (the lower part of the SBD). Thus, wetlands, formed during large-scale pre-PETM sea-level fall, appeared finally drowned and gradually halted to fertilize the basin. The bloom of nannofossil "excursion taxa" and high abundance of *Apectodinium* spp. in the short interval above the SBD indicate the persistence of stress conditions for a short time after the termination of the SBD accumulation.

The termination of enhanced nutrient supply into the basin caused gradual decrease in abundance of eutrophic dinocysts and progressive restoration of pre-PETM nannofossil assemblage. With the disappearance of the highly eutrophic environment and the cessation of TOC accumulation but still during CIE, nannofossils partly recovered their previous abundance. At the same time, negative δ13C values and the persistence of "excursion taxa" of nannofossils and *Apectodinium*-acme beyond the SBD (15–30%) suggest the continuation of the PETM under regionally weakened critical conditions.

In the later phase of the CIE, the increase in $\delta^{18}O$ (samples 715–719, from 0.60 m 1.26 m) corresponds to decrease in abundance of warm-water nannofossil *Discoaster* and dinocyst *Apectodynium* spp. + *Epelidinium pechoricum* complex that more likely suggest the beginning of relative cooling. However, the dramatic increase in $\delta^{18}O$ during the CIE recovery in the interval of samples 721 and 722a (~1.75–2.00 m above the SBD) cannot be easily explained as biotic indications are conflicting: warm-water *Discoaster* shows new trend to increased abundance, while the abundance of *Apectodynium* spp. + *Epelidinium pechoricum* complex progressively decreases. The reduce in abundance of *Apectodynium* spp. + *Epelidinium pechoricum* during the CIE recovery can be rather related to progressive lowering of nutrient availability in the basin, than climatic cooling. The lower abundance of *Homotriblium* spp. also suggests the lower trophication of the basin. The increased abundance of *Spiniferites*-complex likely indicates continued transgressive trend during the CIE recovery.

Despite the restoration during the CIE recovery, nannofossil assemblage remains oppressed at the later stages of this interval: it is characterized by low total abundance, tending to farther reduce up the section, low diversity and very small size of all specimens. This can be related to the beginning of long-lived regression and progressively increasing input of terrestrial siliciclastics (from the level of sample 723 at 2.45 m and father up-section), which led to reduce of light availability and caused the formation of smaller skeletons as adaptation to habitat restricted to shallower depth (Lübke and Mutterlose, 2016).

The SBD represents a regional response to the most critical conditions during the PETM. The progressive recovery of the pre-PETM δ13C values and ratios of the nannofloral and dinocyst communities show that the termination of the PETM was gradual in this part of the Peri-Tethys basin. The restoration of nannofossil and dinocyst assemblages during the later stage of CIE recovery and after CIE termination enables us to suggest that the PETM was not the primary cause of the microplanktonic extinction at the Paleocene/Eocene transition and the re-adaptation to restored "normal" environment appeared to be more critical than paleoecological stress during this event.

Analysis of distribution of TOC, carbon and oxygen isotopes and microfossils within the SBD displays several superimposed types of cyclicity. The increased TOC content and *Apectodinium* abundance and the decline in nannofossil abundance at the base and top of the SBD are likely related to two most pronounced within the SBD transgressive pulses, resulting in the most critical environmental conditions. These two episodes were separated by relative sea-level fall and occurrence less critical conditions during the middle of the SBD (Fig. 13A), as evidenced by lower TOC content, partial recovery of the nannofossil abundance (see Fig. 8) and the relative decline of *Apectodinium*, which was temporarily replaced by *Homotryblium* spp. (see Fig. 10). The smaller-scale variations are associated with four lithological bands and coherent $\delta^{13}C$ variations (Fig. 13B). We documented four similar lithological bands within the SBD of Dzhengutay section, eastern Caucasus, situated more than 300 km eastward from Kheu section (Gavrilov et al., 2009) and similar $\delta^{13}C$ cyclicity is identified within the dissolution horizon of Forada section, Italy (Giusberti et al., 2016) and Site 690, Weddel Sea (Röhl et al., 2007), where they are interpreted as precession cycles. Minor sea-level fluctuations within each lithological band (Fig. 13C) are suggested by variations in nannofossil abundance and peaks in angiosperm pollen, more likely corresponding to relatively brief transgressive pulses (see Figs. 9 and 11). Thus, the cyclicity of different types and orders, which is recognized in the sedimentary record of the Paleocene/Eocene transition of the Kheu section (Fig. 13D), formed the specific lithological architecture of the SBD.

The PETM event is the most dramatic Cenozoic global palaeoecological crisis significantly affected nannofossil evolution, but nannofossil adaptation to critical environmental changes during this event differ fundamentally from their behaviour during mid-Cretaceous Oceanic Anoxic Events (different episodes of OAE1 and OAE2) in the north-eastern Peri-Tethys. The impact of Mesozoic events appeared in the increased nannofossil evolution rate characterized by extinctions prior to the events and origination of new, mainly long-lived, species prior to and after the events. Nannofossil assemblages composed during Mesozoic critical environments demonstrate drastic increase of cosmopolitan *Watznaueria* spp. forming oligotaxonic or even monospecific assemblages, while other species, which were common in the pre-critical epochs, become highly oppressed. The nannofossil response to PETM does not display drastic domination of the few most resistant taxa, but it is expressed in the appearance of short-lived "excursion taxa" adapted to specific conditions during this event. Probably, special effect of PETM on nannofossil evolution is caused by dramatic, but short-term, palaeoecological perturbations and long-term gradual restoration.

6. Conclusion

The high-resolution study of the Paleocene/Eocene transition in the Kheu section revealed the timing of microbiotic and geochemical changes related to PETM. Our results show that the SBD represents the most critical environment during PETM corresponding to the most part of the main body of CIE. The biotic changes derived from the PETM extend over a much larger time span than the sedimentological and geochemical variations detected in the northeastern Peri-Tethys basin. The evolutionary turnover, somehow associated to PETM, is estimated to be occurred during 1 mln interval across the Paleocene/Eocene transition (Aubry, 1998). Some of biotic and abiotic events, documented in the Kheu section, are probably related to global variations (pre-PETM warming, sea-level changes, the occurrence of short-lived *Rhomboaster* and asymmetric *Discoaster* nannofossils, the *Apectodinium*-acme, and the recovery of nannofossil species after the PETM), while others represent regional responses to the global palaeoecological event (the accumulation of TOC-rich sediments, regional development of environmental fluctuations likely caused by orbital cycles, and the occurrence of specific nannofossil and dinocyst assemblages).

The re-appearance of nannofossil species after the PETM and their successive extinction during the recovery period suggest that the slow, long-lasting environmental recovery had a more critical effect on the microbiota than the drastic but brief perturbations caused by the PETM.

Acknowledgements

We are very thankful to Prof. Marie-Pierre Aubry for thorough revision and fruitful discussion helping to improve this paper.We thank Dr. Hans Egger for careful reading of the manuscript and important remarks. This research was supported by the Russian Foundation of Basic Research (Project no. 15-05-07556). This paper is written as a

part of the research on the State Programmes nos. 0135-2014-0070, 0135-2014-0028 and 0135-2014-0024 of the Geological Institute of Russian Academy of Sciences.

References

Aarnes, I., Planke, S., Trulsvik, M., Svensen, H., 2015. Contact metamorphism and thermogenic gas generation in the Vøring and Møre basins, offshore Norway, during the Paleocene–Eocene thermal maximum. J. Geol. Soc. http://dx.doi.org/10.1144/jgs2014-098.

Akhmetiev, M.A., Zaporozhetz, N.I., 1996. Ecosystem Rearrangements Evidenced from the Change in Dinocyst Assemblages in the Paleogene and Lower Miocene of the Russian Platform, Crimea-Caucasian Area, and Turan Plate. In: Kuznetsova, K.I., Muzylöv, N.G. (Eds.), Fossil Microorganisms as a Basis of Stratigraphy, Correlation and Paleogeography. GEOS, Moscow, pp. 55–69 (in Russian).

Alegret, L., Ortiz, S., Orue-Etxebarria, X., Bernaola, G., Baceta, J.I., Monechi, S., Apellaniz, E., Pujalte, V., 2009. The Paleocene-Eocene thermal maximum: new data on microfossil turnover at the Zumaya section, Spain. PALAIOS 24, 318–328.

Alegret, L., Ortiz, S., Arenillas, I., Molina, E., 2010. What happens when the ocean is overheated? The foraminiferal response across the Paleocene–Eocene thermal maximum at the Alamedilla section (Spain). GSA Bull. 122 (9/10), 1616–1624.

Agnini, C., Fornaciari, E., Raffi, I., Catanzariti, R., Pälike, H., Backman, J., Rio, D., 2014. Biozonation and biochronology of Paleogene calcareous nannofossils from low and middle latitudes. Newsl. Stratigr. 47 (2), 131–181.

Angori, E., Bernaola, G., Monechi, S., 2007. Calcareous Nannofossil Assemblages and their Response to the Paleocene/Eocene Thermal Maximum Event at Different Latitudes: ODP 690 Site and Tethyan Sections. In: Monechi, S., Coccioni, R., Rampino, M.R. (Eds.), Large Ecosystem Perturbations: Causes and Concequences, pp. 69–85 Boulder.

Aubry, M.-P., 1992. Late Paleocene calcareous nannoplankton evolution: a tale of climatic deterioration. In: Prothero, N., Berggren, W.A. (Eds.), Eocene–Oligocene Climatic and Biotic Evolution. Columbia University Press, New York, pp. 272–309.

Aubry, M.-P., 1998. Early Paleogene nannoplankton evolution: a tale of climatic amelioration. In: Aubry, M.-P., Lucas, S., Berggren, W.A. (Eds.), Late Paleocene and Early Eocene Climatic and Biotic EvolutionNew York, NY. USA, Columbia University Press, pp. 158–203.

Aubry, M.P., Ouda, K., 2003. Introduction to the upper Paleocene-lower Eocene of the upper Nile Valley: part I stratigraphy. Micropaleontology 49, 15–40.

Aubry, M.-P., Salem, R., 2012. The Dababiya Core: a window into Paleocene to early Eocene depositional history in Egypt based on coccolith stratigraphy. Stratigraphy 9 (3–4), 287–346.

Bains, S., Corfield, R.M., Norris, R.D., 1999. Mechanisms of climate warming at the end of the Paleocene. Science 285, 724–727.

Bannikov, A.F., Carnevale, G., 2012. A long-bodied centriscoid fish from the basal Eocene of Kabardino-Balkaria, northern Caucasus, Russia. Naturwissenschaften 99 (5), 379–389. http://dx.doi.org/10.1007/s00114-012-0912-6.

Beerling, D.J., 2000. Increased terrestrial carbon storage across the Paleocene/Eocene boundary. Palaeogeogr. Palaeoclimatol. Palaeoecol. 161, 395–405.

Bowen, G.J., Maibauer, B.J., Kraus, M.J., Röhl, U., Westerhold, T., Steimke, A., Gingerich, P.D., Wing, S.L., Clyde, W.C., 2014. Two massive, rapid releases of carbon during the onset of the Paleocene–EoceneTthermal maximum. Nat. Geosci. 8, 44–47.

Bown, P.R., Young, J.R., 1998. Techniques. In: Bown, P.R. (Ed.), Calcareous Nannofossil Biostratigraphy. Netherlands Kluwer Academic Publishing, Dordrecht, pp. 16–28.

Bown, P., Pearson, P., 2009. Calcareous plankton evolution and the Paleocene/Eocene thermal maximum event: new evidence from Tanzania. Mar. Micropaleontol. 71 (1–2), 60–70.

Brallower, T.G., 2002. Evidence of surface water oligotrophy during the Paleocene–Eocene thermal maximum: nannofossil assemblage data from ocean drilling program site 690, Maud rise, Weddell Sea. Paleoceanography 17. http://dx.doi.org/10.1029/2001PA000662.

Bralower, T.J., Thomas, D.J., Zachos, J.C., Hirschmann, M.M., Röhl, U., Sigurdsson, H., Thomas, E., Whitney, D.L., 1997. High-resolution records of the late Paleocene thermal maximum and circum-Caribbean volcanism: is there a causal link? Geology 25, 963–967.

Brinkhuis, H., 1994. Late Eocene to early Oligocene dinoflagellate cysts from the Priabonian type-area (Northeast Italy); biostratigraphy and paleoenvironmental interpretation. Palaeogeogr. Palaeoclimatol. Palaeoecol. 107, 121–163.

Bukry, D., 1971. *Discoaster* evolutionary trends. Micropaleontology 17 (1), 43–52.

Bukry, D., 1981. Cenozoic coccoliths from the Deep Sea drilling project. SEPM Spec. Publ. 32, 335–353.

Charles, A.J., Condon, D.J., Harding, I.C., Pälike, H., Marshall, J.E.A., Cui, Y., Kump, L., Croudace, I.W., 2011. Constraints on the numerical age of the Paleocene–Eocene boundary. Geochem. Geophys. Geosyst. 12, Q0AA17. http://dx.doi.org/10.1029/2010GC003426.

Crouch, E.M., Heilmann-Clausen, C., Brinkhuis, H., Morgans, H.E.G., Rogers, K.M., Egger, H., Schmitz, B., 2001. Global dinoflagellate event associated with the late Paleocene thermal maximum. Geology 29, 315–318.

Crouch, E.M., Brinkhuis, H., Visscher, H., Adatte, T., Bolle, M.-P., 2003. Late Paleocene-Early Eocene Dinoflagellate Cyst Records from the Tethys: Further Observations on the Global Distribution of *Apectodinium*. In: Wing, S.L., Gingerich, F.D., Schmitz, B., Thomas, E. (Eds.), Causes and Consequences of Globally Warm Climates in the Early Paleogene. Boulder, Colorado, Geological Society of America Special Paper vol. 369, pp. 113–131.

Crouch, E.M., Brinkhuis, H., 2005. Environmental change across the Paleocene-Eocene transition from eastern New Zealand: a marine palynological approach. Mar. Micropaleontol. 56, 138–160.

Dickens, G.R., O'Neil, J.R., Rea, D.K., Owen, R.M., 1995. Dissociation of oceanic methane hydrate as a cause of the carbon isotope excursion at the end of the Paleocene. Palaeogeography 10, 965–971.

Dickson, A.J., Cohen, A.S., Coe, A.L., Davies, M., Shcherbinina, E.A., Gavrilov, Y.O., 2015. Evidence for weathering and volcanism during the PETM from Arctic Ocean and Peri-Tethys osmium isotope records. Palaeogeogr. Palaeoclimatol. Palaeoecol. 438, 300–307.

Dunkley Jones, T., Lunt, D.J., Schmidt, D.N., Ridgwell, A., Sluijs, A., Valdes, P.J., Maslin, M., 2013. Climate model and proxy data constraints on ocean warming across the Paleocene–Eocene thermal maximum. Earth Sci. Rev. 125, 123–145.

Egger, H., Heilmann-Clausen, C., Schmitz, B., 2009. From shelf to abyss: record of the Paleocene/Eocene-boundary in the eastern alps (Austria). Geol. Acta 7 (1–2), 215–227.

Egger, H., Homayoun, M., Huber, H., Rögl, F., Schmitz, B., 2005. Early Eocene climatic, volcanic, and biotic events in the northwestern Tethyan UnterSBDerg section, Austria. Palaeogeogr. Palaeoclimatol. Palaeoecol. 217, 243–264.

Eldholm, O., Thomas, E., 1993. Environmental impact of volcanic margin formation. Earth Planet. Sci. Lett. 117 (3–4), 319–329.

Erba, E., Bottini, C., Weissert, H.J., Keller, C.E., 2010. Calcareous nannoplankton response to surface-water acidification around oceanic anoxic event 1a. Science 329, 428–432.

Fricke, H.C., Clyde, W.C., O'Neil, J.R., Gingerich, P.D., 1998. Evidence for rapid climate change in North America during the latest Paleocene thermal maximum: oxygen isotope compositions of biogenic phosphate from the Bighorn Basin (Wyoming). Earth Planet. Sci. Lett. 160, 193–208.

Fuqua, L.M., Bralower, T.J., Arthur, M.A., Patzkowsky, M.E., 2008. Evolution of calcareous nannoplankton and the recovery of marine food webs after the cretaceous-Paleocene mass extinction. PALAIOS 23 (4), 185–194.

Galeotti, S., Angori, E., Coccioni, R., Ferrari, G., Calbrun, B., Monechi, S., Premoli Silva, I., Speijer, R., Turi, B., 2000. Integrated stratigraphy across the Paleocene/Eocene boundary in the Contessa road section, Gubbio (Central Italy). Bull. Soc. Geol. Fr. 171 (3), 355–365.

Lu, G., Keller, G., Adatte, T., Ortiz, N., Molina, E., 1996. Long term (10^5) and short term (10^3) δ13C excursion near the Paeocene/Eocene transition: evidence from the Tethys. Terra Nova 8, 347–355.

Gavrilov, Y.O., Kodina, L.A., Lubchenko, I.Y., Muzylöv, N.G., 1997. The late Paleocene anoxic event in epicontinental seas of Peri-Tethys and formation of sapropelite unit: sedimentology and geochemistry. Lithol. Miner. Resour. 35, 427–450.

Gavrilov, Y.O., Muzylöv, N.G., 1991. The geochemistry of sapropelitic interbeds in Paleogene of the central Caucasus. Lithol. Miner. Resour. 26, 548–559.

Gavrilov, Y.O., Shcherbinina, E.A., Muzylöv, N.G., 2000. A Paleogene sequence in central north Caucasus: a response to paleoenviromental changes. GFF 122, 51–53.

Gavrilov, Y., Shcherbinina, E., Golovanova, O., Pokrovsky, B., 2009. A Variety of PETM Records in Different Settings of Northeastern Peri-Tethys. In: Crouch, E.M., Strong, C.P., Hollis, C.J. (Eds.), Climatic and Biotic Events of the Early Paleogene (CBEP 2009). Extended Abstracts from an International Conference, Wellington, New Zealand, 12–15 January 2009. GNS Science Miscellaneous Series vol. 18, pp. 67–70.

Gavrilov, Y.O., Shcherbinina, E.A., Oberhänsli, H., 2003. Paleocene/Eocene Boundary Events in the Northeastern Peri-Tethys. In: Wing, S.L., Gingerich, F.D., Schmitz, B., Thomas, E. (Eds.), Causes and Consequences of Globally Warm Climates in the Early Paleogene. Boulder, Colorado, Geological Society of America Special Paper vol. 369, pp. 147–168.

Gibbs, S.J., Stoll, H.M., Bown, P.R., Bralower, T.J., 2010. Ocean acidification and surface water carbonate production across the Paleocene-Eocene thermal maximum. Earth Planet. Sci. Lett. 295, 583–592.

Gibbs, S.J., Bown, P.R., Murphy, B.H., Sluijs, A., Edgar, K.M., Palike, H., Bolton, C.T., Zachos, J.C., 2012. Scaled biotic disruption during early Eocene global warming events. Biogeosciences 9, 4679–4688.

Giusberti, L., Boscolo Galazzo, F., Thomas, E., 2016. Variability in climate and productivity during the Paleocene–Eocene thermal maximum in the western Tethys (Forada section). Clim. Past 12 (2), 213–240.

Handley, L., Crouch, E.M., Pancost, R.D., 2011. A New Zealand record of sea level rise and environmental change during the Paleocene–Eocene thermal maximum. Palaeogeogr. Palaeoclimatol. Palaeoecol. 305, 185–200.

Handley, L., O'Halloran, A., Pearson, P.N., Hawkins, E., Nicholas, C.J., Schouten, S., McMillan, I.K., Pancost, R.D., 2012. Changes in the hydrological cycle in tropical East Africa during the Paleocene–Eocene thermal maximum. Palaeogeogr. Palaeoclimatol. Palaeoecol. 329–330, 10–21.

Haq, B.U., Hardenbol, J., Vail, P.R., 1987. Chronology of Fluctuating Sea levels since the Triassic. Science 235, 1156–1167.

Hay, W.W., 1970. Calcareous Nannofossils from Cores Recovered on Leg 4. Initial Reports of DSDP. 4, pp. 455–501.

Hereid, K., 2007 (unpublished). *Pyrodinium bahamense var. bahamense* cysts as a dinoflagellate population and depositional environment proxy in Puerto Mosquito, Vieques, Puerto Rico. Submitted in partial fulfillment of the requirements for the Bachelor of Arts degree in Geology, Carleton College, Northfield, Minnesota.

Higgins, P., 2012. Climate change at the Paleocene/Eocene boundary: new insights from mollusks and organic carbon in the Hanna Basin of Wyoming. Palarch's J. Vertebr. Palaeontol. 9 (4), 1–20.

Hilgen, F.J., Kuiper, K.F., Lourens, L.J., 2010. Evaluation of the astronomical time scale for the Paleocene and earliest Eocene. Earth Planet. Sci. Lett. 300, 139–151.

Kahn, A., Aubry, M.-P., 2004. Provincialism associated with the Paleocene/Eocene thermal maximum: temporal constraint. Mar. Micropaleontol. 52, 117–131.

Khozyem, H., Adatte, T., Spangenberg, J.E., Tantawi, A.A., Keller, G., 2013. Palaeoenvironmental and climatic changes during the Palaeocene–Eocene Thermal Maximum (PETM) at the Wadi Nukhul Section, Sinai, Egypt. J. Geol. Soc. Lond. 170, 341–352.

Khozyem, H., Adatte, T., Keller, G., Tantawy, A.A., Spangenberg, J.E., 2014. The Paleocene-Eocene GSSP at Dababiya, Egypt – revisited. Episodes 37 (2), 78–85.
Khozyem, H., Adatte, T., Spangenberg, J.E., Keller, G., Tantawy, A.A., Ulianov, A., 2015. New geochemical constraints on the Paleocene–Eocene thermal maximum: Dababiya GSSP, Egypt Palaeogeogr. Palaeoclimatol. Palaeoecol. 429, 117–135.
Paleogeographic Maps on the Palinspastic Reconstruction. In: Kazmin, V.G., Natapov, L.G. (Eds.), Institute of the Tectonics of Lithosphere Plates. Russian Academy of Natural Sciences CD edition in a memory of Lev Zonenhain.
Kelly, D.C., Bralower, T.J., Zachos, J.C., Premoli Silva, I., Thomas, E., 1996. Rapid diversification of planktonic foraminifera in the tropical Pacific (ODP site 865) during the late Paleocene thermal maximum. Geology 24, 423–426.
Kenett, J.P., Stott, L.D., 1991. Abrupt deep sea warming, paleoceanographic changes and bentic extinctions at the end of Paleocene. Nature 353, 225–229.
Kodina, L.A., Gavrilov, Y.O., Jones, M., Eglinton, G., 1995. Environment of Upper Paleocene Black Shale Deposition in Southern Russia and Adjacent Regions as Revealed by Isotope and Biomarker Study. Organic Geochemistry: Developments and Applications to Energy, Climate, Environment and Human HistorySelected Papers from the 17th Intern. Meeting on Organic Geochemistry. Donostia-San Sebastian, The Basque Country. Spain, pp. 192–194 4-8th Sept. 1995.
Lees, J.A., Bown, P.R., Mattioli, E., 2005. Problems with proxies? Cautionary tales of calcareous nannofossil paleoenvironmental indicators. Micropaleontology 51 (4), 333–343.
Lübke, N., Mutterlose, J., 2016. The impact of OAE 1a on marine biota deciphered by size variations of coccoliths. Cretac. Res. 61, 169–179.
Luterbacher, H.P., Ali, J.R., Brinkhuis, H., Gradstein, F.M., Hooker, J.J., Monechi, S., Ogg, J.G., Powell, A.J., Röhl, U., Sanfilippo, A., Schmitz, B., 2004. The Paleogene Period. In: Gradstein, F.M., Ogg, J.G., Smith, A.G. (Eds.), A Geologic Time Scale 2004. Cambridge University Press, Cambridge, pp. 384–408.
Manners, H.R., Grimes, S.T., Sutton, P.A., Domingo, L., Leng, M.J., Twitchett, R.J., Hart, M.B., Dunkley Jones, T., Pancost, R.D., Duller, R., Lopez-Martinez, N., 2013. Magnitude and profile of organic carbon isotope records from the Paleocene–Eocene thermal maximum: evidence from northern Spain. Earth Planet. Sci. Lett. 376, 220–230.
Martini, E., 1971. Standard Tertiary and Quaternary calcareous nannoplankton zonation. In: Farinacci, A. (Ed.), Proceedings of the 2nd Planktonic Conference on Planktonic Microfossils Roma. Tecnoscienza, Roma 2, pp. 739–785.
Monechi, S., Angori, E., Speijer, R., 2000. Upper Paleocene biostratigraphy in the Mediterranean region: zonal markers, diachronism, and preservational problems. GFF 122, 108–110.
Muzylöv, N.G., 1994. Paleocene-Middle Eocene Anoxic Events. In: Rozanov, A.V. (Ed.), Ecosystem Reorganization and Biosphere Evolution. 1, pp. 160–166 Moscow, Nedra. (in Russian).
Pagani, M., Caldeira, K., Archer, D., Zachos, J.C., 2006. An ancient carbon mystery. Science 314, 1556–1557.
Pälike, H., Lyle, M.W., Nishi, H., et al., 2012. A Cenozoic record of the equatorial Pacific carbonate compensation depth. Nature 488, 609–615.
Penman, D.E., Hönisch, B., Zeebe, R.E., Thomas, E., Zachos, J.C., 2014. Rapid and sustained surface ocean acidification during the Paleocene-Eocene thermal maximum. Paleoceanography 29 http://dx.doi.org/10.1002/2014PA002621.
Powell, A.J., 1992. Dinoflagellate Cysts of the Tertiary System. In: Powell, A.J. (Ed.), A Stratigraphic Index of Dinoflagellate Cysts. British Micropaleontological Society Publication Series, Chapman & Hall, pp. 155–251.
Powell, A.J., Brinkhuis, H., Bujak, J.P., 1996. Upper Paleocene-Lower Eocene Dinoflagellate Cyst Sequence Biostratigraphy of Southeast England. In: Knox, R.W.O.B., Corfield, R.M., Dunay, R.S. (Eds.), Correlation of the Early Paleogene in Northwest Europe: Geological Society Special Publication. 101, pp. 145–183.
Pujalte, V., Schmitz, B., Baceta, J.I., 2014. Sea-level changes across the Paleocene–Eocene interval in the Spanish Pyrenees, and their possible relationship with North Atlantic magmatism. Palaeogeogr. Palaeoclimatol. Palaeoecol. 393, 45–60.
Raffi, I., Backman, J., Zachos, J.C., Sluijs, A., 2009. The response of calcareous nannofossil assemblages to the Paleocene Eocene thermal maximum at the Walvis ridge in the South Atlantic. Mar. Micropaleontol. 70, 201–212.
Radionova, E.P., Aleksandrova, G.N., Gavtadze, T.T., Stupin, S.I., Khokhlova, I.E., 2009. Analysis of Late Paleocene-Early Eocene Micropankton from the Kheu River Section, West Pre-Caucasus. In: Crouch, E.M., Strong, C.P., Hollis, C.J. (Eds.), Climatic and Biotic Events of the Paleogene (CBEP 2009). Extended Abstracts from an International Conference in Wellington, New Zealand, 12–15 January 2009. GNS Science Miscellaneous Series Vol. 18, pp. 111–116.
Reinchart, G.-L., Brinkhuis, H., Huiskamp, F., Zachariasse, W.J., 2004. Hyperstratification following glacial overturning events in the northern Arabian Sea. Paleoceanography 19 (2). http://dx.doi.org/10.1029/2003PA000900.
Riebesell, U., Zondervan, I., Rost, B., Tortell, P.D., Zeebe, R.E., Morel, F.M.M., 2000. Reduced calcification of marine plankton in response to increased atmospheric CO2. Nature 407, 364–367.
Röhl, U., Westerhold, T., Bralower, T.J., Zachos, J.C., 2007. On the duration of the Paleocene-Eocene thermal maximum (PETM). Geochem. Geophys. Geosyst. 8 (2), Q12002. http://dx.doi.org/10.1029/2007GC001784.
Romein, A.J.T., 1979. Lineages in early Paleogene calcareous nannoplankton. Utrecht Micropaleontol. Bull. 22 (231 pp.).
Secord, R., Gingerich, P.D., Lohmann, K.C., Macleod, K.G., 2010. Continental warming preceding the Paleocene–Eocene thermal maximum. Nature 467, 955–958.
Self-Trail, J.M., Powars, D.S., Watkins, D.K., Wandless, G.A., 2012. Calcareous nannofossil assemblage changes across the Paleocene–Eocene thermal maximum: evidence from a shelf setting. Mar. Micropaleontol. 92–93, 61–80.
Sluijs, A., Bijl, P.K., Schouten, S., Röhl, U., Reinchart, G.-L., Brinkhuis, H., 2010. Southern Ocean warning and hydrological change during the Paleocene–Eocene thermal maximum. Clim. Past 6, 1701–1731. http://dx.doi.org/10.5194/cpd6-1701-2010.
Sluijs, A., Bowen, G., Brinkhuis, H., Lourens, L., Thomas, E., 2007. The Paleocene–Eocene Thermal Maximum Super Greenhouse: Biotic and Geochemical Signatures, Age Models and Mechanisms of Global Change. In: Williams, M., Haywood, A.M., Gregory, F.J., Schmidt, D.N. (Eds.), Deep-Time Perspectives on Climate Change: Marrying the Signal from Computer Models and Biological Proxies. Geol. Soc. Spec. Publ., London, pp. 323–349.
Sluijs, A., Brinkhuis, H., 2009. A dynamic climate and ecosystem state during the Paleocene–Eocene thermal maximum: inferences from dinoflagellate cyst assemblages on the New Jersey shelf. Biogeosciences 6, 5163–5215. http://dx.doi.org/10.519/bg-6-5163-2009.
Sluijs, A., Brinkhuis, H., Crouch, E.M., et al., 2008. Eustatic variations during the Paleocene–Eocene greenhouse world. Paleoceanigraphy 23. http://dx.doi.org/10.1029/2008PA001615.
Sluijs, A., Pross, J., Brinkhuis, H., 2005. From greenhouse to icehouse; organic-walled dinoflagellate cysts as paleoenvironmental indicators in the Paleogene. Earth Sci. Rev. 68, 281–315.
Sluijs, A., Schouten, S., Pagani, M., Woltering, M., Brinkhuis, H., Sinninghe Damsté, J.S., Dickens, J.R., Huber, M., Reinchart, G.-L., Stein, R., Mattiessen, J., Lourens, L.J., Pedentchouk, N., Backman, J., Moran, K., the Expedition 302 Scientists, 2006. Subtropical Arctic Ocean temperatures during the Paleocene/Eocene thermal maximum. Nature 441, 610–613.
Smith, F.A., Wing, S.L., Freeman, K.H., 2007. Magnitude of the carbon isotope excursion at the Paleocene–Eocene thermal maximum: the role of plant community change. Earth Planet. Sci. Lett. 262, 50–65.
Speijer, R.P., Schmitz, B., Van der Zwaan, G.L., 1997. Benthic foraminiferal extinction and repopulation in response to latest Paleocene Tethyan anoxia. Geology 25 (8), 683–686.
Speijer, R.P., Wagner, T., 2002. Sea-level changes and black shales associated with the late Paleocene thermal maximum: organicgeochemical and micropaleontologic evidence from the southern Tethyan margin (Egypt–Israel). Geol. Soc. Am. Spec. Pap. 356, 533–549.
Speijer, R.P., Scheibner, C., Stassen, P., Morsi, A.-M., 2012. Response of marine ecosystems to deep-time global warming: a synthesis of biotic patterns across the Paleocene–Eocene thermal maximum (PETM). Aust. J. Earth Sci. 105 (1), 6–16.
Stupin, S.I., 2008. Paleocene/Eocene foraminiferal assemblages in the central part of northern Caucasus. Geol. Geophys. 49, 357–359 (in Russian).
Stupin, S.I., Muzylöv, N.G., 2001. The late Paleocene ecologic crisis in epicontinental basins of the eastern Peri-Tethys: microbiota and accumulation conditions of sapropelitic bed. Stratigr. Geol. Correl. 9 (5), 501–507.
Svensen, H., Planke, S., Malthe-Sørenssen, A., Jamtveit, B., Myklebust, R., Rasmussen Eidem, T., Rey, S.S., 2004. Release of methane from a volcanic basin as a mechanism for initial Eocene global warming. Nature 429, 542–545.
Thomas, D.J., Zachos, J.C., Bralower, T.J., Thomas, E., Bohaty, S., 2002. Warming the fuel for the fire: evidence for the thermal dissociation of methane hydrate during the Paleocene-Eocene thermal maximum. Geology 1067–1070.
Thomas, E., Zachos, J.C., Bralower, T.J., 2000. Deep-Sea Environments on a Warm Earth: Latest Paleocene–Early Eocene. In: Huber, B., MacLeod, K., Wing, S. (Eds.), Warm Climates in Earth History. Cambridge University Press, Cambridge, United Kingdom, pp. 132–160.
Tipple, B.J., Pagani, M., Krishnan, S., Dirghangi, S.S., Galeotti, S., Agnini, C., Giusberti, L., Rio, D., 2011. Coupled high-resolution marine and terrestrial records of carbon and hydrologic cycles variations during the Paleocene–Eocene thermal maximum (PETM). Earth Planet. Sci. Lett. 311, 82–92.
Zachos, J.C., Röhl, U., Schellenberg, S.A., Sluijs, A., Hodell, D.A., Kelly, D.C., Thomas, E., Nicolo, M., Raffi, I., Lourens, L.J., McCarren, H., Kroon, D., 2005. Rapid acidification of the ocean during the Paleocene–Eocene thermal maximum. Science 308, 1611–1615.